Numerical and experimental investigation of microparticles manipulation using a developed two-stage acoustofluidics platform

By

Mohammadamin Heydari

B.Sc., K.N. Toosi, University of Technology, Iran, 2015

A Thesis Submitted in Partial Fulfillment of the

Requirements for the Degree of

Master of Applied Science

in the Department of Mechanical Engineering

University of Victoria

Supervisory Committee

Numerical and experimental investigation of microparticles manipulation using a developed two-stage acoustofluidics platform

By

Mohammadamin Heydari

B.Sc., K.N. Toosi University of Technology, Iran, 2015

Supervisory committee

Dr. Mina Hoorfar, Supervisor
Department of Mechanical Engineering

Dr. Mohsen Akbari, Departmental Member
Department of Mechanical Engineering,

Abstract

As blood circulates throughout the body, it delivers different nutrients and oxygen and removes waste. Numerous blood cells characterize the physiological condition of the body and changes in the quantity and condition of blood cells can result in disease; thus, the isolation of certain blood cells can aid in the diagnosis and treatment of various diseases.

Conventional techniques for blood cell separation are time-consuming, costly, and can result in morphological changes due to high shear stress. Innovative lab-on-a-chip-based separation techniques have been utilized to solve these issues. Acoustofluidics (i.e., a coupling of microfluidics and acoustics) has been one of the most effective approaches for separating cells, EVs, and synthetic microparticles among the different methods introduced. In contrast to conventional separation procedures used in clinical laboratories, which are focused on chemical qualities, the acoustofluidic process depends on the sample's physical properties. Studies working on blood cell separation using acoustophoretic technique are mostly limited to separation/purifying RBC and Platelets. In contrast, the separation of different subtypes of WBCs has not been investigated thoroughly since the cutoff size of different types of white blood cells is narrow. Thus, separating such cells requires enhanced precision, significantly if the method used is only sized-based. This work studies the potential of using a two-stage parallel standing surface acoustic wave (paSSAW) acoustofluidic platforms in separating microparticles with small cutoff sizes. The first stage of the device employs a combination of acoustic and hydrodynamic focusing mechanisms to boost the alignment efficiency prior to the second stage. The second module of the device separates the microparticles using a paSSAW acoustofluidics platform. In this thesis, a three-dimensional numerical simulation has been developed to maximize the performance of the platforms mentioned above and study the effect of different design parameters on the precision of the separation. The

numerical results were then validated by a subsequent experimental study. In complete agreement with the numerical result, the developed platform achieved a high-resolution separation of 2 μm cutoff size where 10μm and 8μm diameter polystyrene microparticles were successfully separated with an accepted rate of purity of >80%.

Keywords: acoustofluidics, microparticle separation, surface acoustic wave (SAW), parallel standing surface acoustic wave (paSSAW), pressure node (PN), pressure anti node (PAN), acoustic radiation force (ARF), interdigital transducer (IDT)

Table of Contents

List of Figures

List of Tables

List of symbols and abbreviations

D	Particles diameter
$\dot{Q}_{Sample}$	Sample flow rate (flowrate of the main flow containing particles)
$\dot{Q}_{Sheath}$	Sheath flow rate
$P_{acoustic}$	Acoustic pressure
F_r	Acoustic radiation force
F_d	Drag force
W_C	Width of the microchannel
H_C	Height of the microchannel
W_P	Thickness of the PDMS wall
λ_{SAW}	Wavelength of the Acoustic Wave
d_{IDT}	Distance between IDTs
Δd_x	Lateral distance between particles at the separation stage
QF	Quality factor
NF	Number of fingers in each interdigital transducer design
PN	Pressure node
PAN	Pressure anti-node
SAW	surface acoustic wave
SSAW	Standing surface acoustic wave
paSSAW	Parallel standing surface acoustic wave
IDT	Interdigital transducer

Acknowledgements

I would like to express my deepest appreciation to my supervisor, Dr. Mina Hoorfar, for all her support during my master's journey. I would like to express my gratitude to my amazing lab manager Nishat Tasnim for all of her support. I would also like to express my gratitude to all my fellow lab mates for their help and support.

Dedication

I would like to dedicate this thesis to my parents and my beloved sister. I am grateful to you for getting me started on this path of continuous education, and always believing in me. I always consider myself a lucky person to be born in such a lovely family.

Chapter 1: Introduction

1.1 Bioparticle separation/isolation

Separating individual chemicals from mixtures has been utilized in numerous domains, including biological study, spectrometry, and the detection of disease[1]. In recent decades, the separation of cells and bioparticles for various biological and medicinal applications has received increased attention. Certain diseases are diagnosed based on the detection of pertinent pathogens or cells, and the successful isolation of these particles is a crucial prerequisite for correct detection. Isolation, separation, and focusing of bioparticles are foundational processes in many of these fields of application [2], [3]. Several traditional separation techniques have been used to perform this objective for a very long time[4]. These methods take advantage of variations in the cells form, size, density, and conductivity[5]. Immunoassay cell separation[6], fluorescence-activated cell sorting)[7],and density gradient centrifugation[8] are all examples of well-established methods frequently used in cell biology applications. Nevertheless, they need lengthy processing times, vast volumes of specimens and chemicals, and have been linked to human mistakes [9].

1.1.1 Microfluidics bioparticle/cell separation

In recent decades, improvements in the development of lab-on-a-chip (LOC) technologies have made it feasible to do a complete or partial experiment on devices barely larger than a smartphone[10]. Using diverse techniques, microfluidic devices might be easily produced and linked with various systems. In addition, the flow pattern is laminar and has less complexity, which enhances flow control and simplifies the procedures. As the channel scale is diminished, fewer samples and reagents are needed for assessment[11]. These technologies have been widely used in various applications, including diagnostics[12], proteomics[13], and cell-based research[14], [15].

According to the separation principle, microfluidics-based devices can be generally split into two groups: passive and active techniques. Passive separation methods include microstructural filtration [16], deterministic lateral migration[17], hydraulic[18], and inertia-based separation methods [19]. Passive separation methods utilize a specifically engineered channel or fluid flow to alter the direction of particles. In contrast, active separation techniques utilize an external field, including electrical[20], magnetic [21], acoustic [22], and optical [23] fields, to impose a force on particles and cells to separate them. Compared to active methods, passive methods offer greater throughput and are easier to fabricate. Although, passive approaches for separating biomolecules have been found to result in a lower purity than active methods [24]. Active methods offer a wide variety of advantages. They are non-invasive (contactless), label-free (since it is not necessary to use antibodies or beads in most cases), and show better biocompatibility, which allows the integrity, functionality, and viability of cells and biological compounds to be perfectly preserved during the process. Also, they can manipulate particles and cells within simple and low-cost microchannels[25].

All the mentioned active isolation techniques depend on the microparticles' size. However, it should be mentioned that similarities in the electrical characteristic of the microparticles and the medium substantially reduce the effectiveness of the electrically based separation method [26]. Furthermore, the magnetic-based manipulation technique can only be utilized if the particles are magnetic[27].

Particularly, the acoustofluidic-based cell manipulation approaches address and resolves these challenges, since it is the only active method that operates on the basis of mechanical qualities as opposed to electrical or magnetic characteristics. acoustofluidics is promising technology that combines

acoustic radiation waves in microfluidic platforms to manipulate particles and fluid in micro scale. In addition, it has proven to be a promising method for the isolation/recovery of bioparticles due to its low cost, simple fabrication, label-free and contact-free microparticle manipulation, excellent biocompatibility, and stability [28], [29].

1.1.2 Applications of acoustophoretic in bioparticle separations

The term acoustofluidics refers to the use of ultrasonic waves in microfluidic systems. On the basis of the acoustic wave guiding technique, acoustofluidic platforms can be divided into two categories [30], [31]: Surface Acoustic Wave (SAW) [32], and Bulk acoustic Wave (BAW[33]).

SAW has been widely used for many biological applications, whereas BAW is confined to applications requiring high frequencies[34]. Surface acoustic waves are mechanical waves that travel primarily along the surface of an elastic substance. These waves combine a longitudinal compression movement with a transverse shear movement having wave vectors orthogonal to the surface normal direction [35], [36]. In SAWs The waves are generated by interdigital transducers (IDTs) [37], which are comb-shaped electrodes patterned on a piezoelectric material's surface, and their transmission continues until they reach the PDMS-made microchannel.

SAW-based bioparticle manipulation has been efficiently implemented in a variety of microfluidic applications, including blood cells separation [38]–[41], separation of cancer cells [42], [43], separation of bacteria and virus [44], [45], separation/purification of proteins [46], separation of exosomes [47], [48].

The symptoms of a bacterial infection can be quite severe at times. In order to confirm a diagnosis and determine what kind of bacteria is responsible for an infection, rapid and efficient isolation of bacteria from complex body fluids is essential. Ning et al.[49] created a serpentine acoustofluidic device for separating E. coli bacteria from white blood cells. By enclosing samples

in an acoustic field, their device increased the action length and allowed a greater flow rate. Because the ARF was weaker, the smaller bacteria stayed in the middle of the channel, while the larger WBCs moved to the pressure nodes, each exiting the channel through a different location. The result demonstrated a separation purity of 92.7% and a flow rate of 25 mm s-1, which are superior to those reported for similar devices.

In another work on bacteria separation Sixing Li et al. [50] presented an acoustofluidic device for the separation of Escherichia coli (E. coli) from human blood samples by use of the tilted-angle standing surface acoustic wave (taSSAW) technique based on the size difference between E. coli and blood cells. The purity of the E. coli isolated from red blood cells is greater than 96%, as determined by flow cytometry. Because of the elimination of blood cells, the label-free electrochemical detection of the separated E. coli shows fewer non-specific signals.

Using a microfluidic device and standing surface acoustic waves (SSAWs) Jeonghun Nam et al. [51] presented a way to isolate platelets from undiluted whole blood. Microfluidic channels made of polydimethylsiloxane (PDMS) were combined with interdigitated transducer (IDT) electrodes patterned on a piezoelectric substrate. Flow cytometric analysis revealed that the RBC clearance ratio in whole blood was greater than 99.9% and platelets had a purity level of approximately 98%.

In order to separate particles based on the intensity of the acoustic radiation force, it is common practice to focus them along the wall of the channel and then expose them to the force. The particles travel laterally towards the pressure nodes, which are typically located in the middle of the channel because the acoustic field is orthogonal to the flow. Particles of varying sizes can be directed to distinct exits by modifying the channel's flow rate, width, and length in addition to the acoustic wave's intensity. Chen et al. [52] demonstrated that this method can separate platelets

from whole blood at a high throughput. Their device, operating at a flow rate of 10 mL min1, was able to separate more than 85% of WBCs and RBCs and recover more than 80% of platelets. Whole blood samples are introduced at the lower end of the device and guided to the area around the pressure antinodes. The acoustic force lifts all particles, but the larger RBCs and WBCs feel it more strongly than the smaller platelets do. Consequently, they accelerate toward the upper channel and dissociate from the platelets.

1.2 Motivations

Studies working on blood cell separation using acoustophoretic techniques are mostly limited to separation/purifying RBC and Platelets [53] whereas separation of different subtypes of WBCs has not been investigated thoroughly due to the fact that the cutoff size of different types of white blood cells is narrow hence separating such cells requires enhanced precision especially if the method being used is only sized based [54].

Hence, the primary motivation of this work is to investigate the feasibility of the proposed two-stage paSSAW acoustophoretic design to reduce the cutoff size of microparticle separation with the potential application of separating subtypes of WBCs or other close-range size bioparticles. In this study, we have employed a 3D numerical model using COMSOL software to investigate the effect of IDT and channel configuration in the efficiency of particle separation. Moreover, most of the numerical studies on microparticle manipulation are limited to 2D/1D simulation which cannot provide the proper solution for precisely studying the mechanism of microparticles separation.

Many studies solely explored a 1D harmonic standing waves modeling method to model the fluid's acoustic pressure distribution numerically[55]–[57]. The 1D HSW model is incapable of computing the actual acoustic pressure variation within the microchannel. When SSAW leaks into the fluid and PDMS domains, longitudinal waves are mostly responsible for the disparity between the actual result and that predicted by 1D HSW. Fundamentally, the mismatch in acoustic impedances between PDMS and the fluid is responsible for the acoustic energy reflection caused by longitudinal waves. In this context, an accurate representation of the acoustic pressure variation arising from SSAW within the microfluidic channel is particularly desirable [58].

Several attempts have been made to enhance the precision of numerical simulations by including 2D modelling. Using a 2D numerical simulation, Nitesh et al. [59]determined the first-order fields that drive acoustic streaming along with the time-averaged acoustic emission forces applying on suspended particles. However, they reduced the system by leveraging the piezoelectric substrate's action rather than representing it as a separate domain. As a result of ignoring the piezoelectric's internal energy dissipation, this approximation adds an inherent bias to the computed acoustic pressure. In a separate investigation, Hsu et al. [60] studied the application of dual-wavelength SSAW for directing the migratory of microparticles towards the microchannel. However, this research was restricted to the fluid domain, and the impact of the PDMS walls and the piezoelectric zone were not fully comprehended.

Therefore, numerical models can be utilized to allow for the influence of channel components (materials and rotations) in the SAW path. Because walls are an integral part of these devices, it is crucial to relate particle actuation to the channel configuration instead of underlying SAW, enabling highly targeted patterning and focusing behaviors that can be integrated by altering the channel characteristics[61]. Moreover, proper evaluation of microparticles behaviors in

acoustophoretic applications not only requires modeling the PDMS walls but also proper 3D modeling is needed to account for designing the proper channel length as well as calculating the lateral displacement of micro particles.

All the mentioned limitations of prior studies necessitate additional work in order to acquire insight into acoustophoretic-based microparticle manipulation and improve the early design elements of acoustofluidic chips. By utilizing the optimal parameters used in the design of the acoustofluidic chip, particle/cell manipulation and separation would be accomplished in a highly accurate and controllable manner.

.

1.3 Objective

1- Implementing a 3D numerical model for the parametric study of the effect of various operational conditions and device attributes. In order to conduct a numerical simulation of the paSSAW field, the optimal values for the operational circumstances and geometry are determined using first-order equations. After computing the optimal values, the trajectories of microparticles of various sizes are examined.

2- Using experimental testing conducted under the same conditions to validate the numerical simulation.

3- Utilizing the proven optimal values in the acoustofluidic chip's final design. This step focuses on determining the separation efficiency of microparticles of various sizes.

Chapter 2: Background theory and working principle

2.1 Piezoelectricity background theory

There are numerous techniques for producing ultrasonic waves, including piezoelectric [62], electrostriction [63], magnetostriction [64] and electromagnetic [65]. The piezoelectric-based approach is widely employed in the excitation of ultrasonic waves in SAW-based microfluidic devices due to its capacity to generate highly repeatable complicated form and frequency content waves, as well as excite diverse wave modes [66]. In addition, piezoelectric transduction provides substantial forces at low strain rates for manipulation, as well as relatively high voltages and low currents for detecting [66].

To create piezoelectric waves, a crystal free of a symmetry center is required. Mechanical and electrical properties of piezoelectric materials exhibit high anisotropy. Consequently, a mechanical displacement field is produced by the fluctuation in surface charge density on the crystal face. SAW features both transverse and longitudinal mechanical displacement components moving near the surface of the piezoelectric material. SAW can generate a broad spectrum of frequencies from MHz to GHz, which reduces the acoustic wavelength and enhances the performance of such devices [67].

Lithium niobate (LiNbO3) is the most common material utilized to fabricate SAW devices. Low acoustic attenuation and temperature coefficient of delay, as well as impulsive polarization and high acoustic velocity have made the LiNbo3 the preferred material in surface acoustic wave applications [68]

2.2 Interdigital Transducer (IDT) configuration

To produce surface acoustic waves (SAWs), an electric alternating current (AC) signal with a resonant frequency is delivered to an acoustic wave production element known as an interdigitated transducer (IDT) [69]

IDTs consist of comb-pattern metal electrodes placed on a piezoelectric material to transmit electrical energy to mechanical energy [70]

The size and shape of IDTs must be tuned to enable activation at the resonance frequency, thus enhancing the durability and reproductivity of SAWs and maximizing the conversion of electric energy to mechanical power [71]. As shown in Figure 1, the most fundamental IDT design consists of two parallel sets of rectangular metal fingers that are spatially periodic. The frequency of the finger pairs (pitch) determines the wavelength of the generated SAW, so that the space between each pair of fingers is $\lambda_{SAW}/4$.

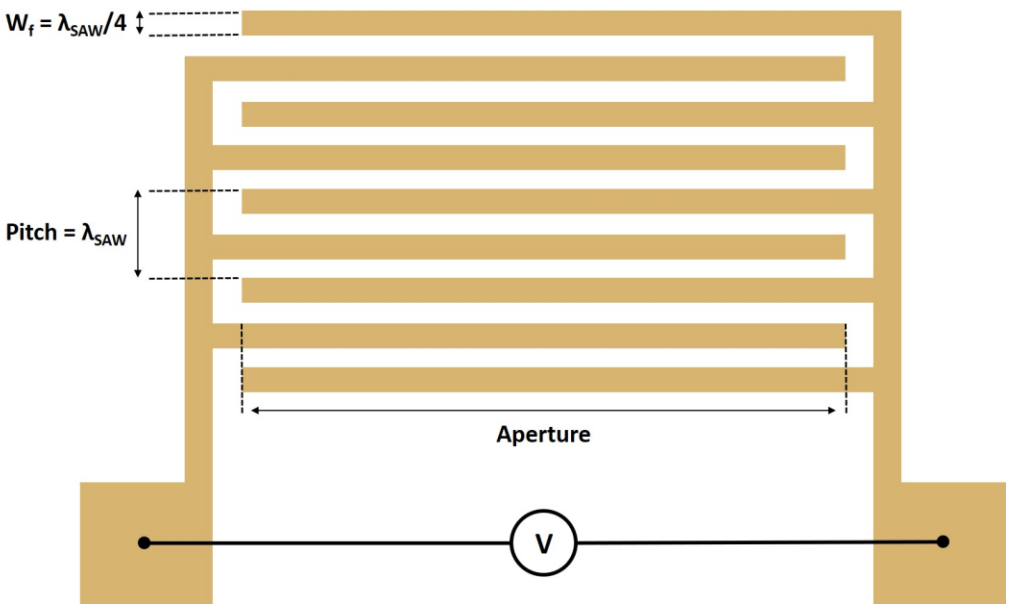

Figure 1) Schematic of the interdigitated electrode configuration parameters

To produce steady Rayleigh waves, the IDT pitch must correspond to the SAW wavelength (λ_{SAW}). The speed of sound in piezoelectric crystals (c_{Piezo}) is related to the material parameters of the substrate and the direction of sound propagation. Consequently, the resonance frequency of a specific device is governed by the substrate, IDT configuration, and propagation direction, which can be represented as:

$$f_0 = \frac{c_{Piezo}}{\lambda_{SAW}} \qquad \text{Eq. 2.1}$$

2.3 Acoustic radiation force working principles

When SAW waves encounter a liquid or solid medium, they are transformed into leaky surface acoustic waves [72]. Through the viscous damping generated by the acoustic streaming flow (ASF) in the fluid, the propagating LSAW decelerates and delivers an acoustic radiation force (ARF) to micron size particles. SAW that is emitted away from the IDT is known as a traveling surface acoustic wave (TSAW), whereas a standing surface acoustic wave (SSAW) is formed whenever two identical traveling SAWs spread in opposite directions and interfere effectively [73]. Both forms of SAW generate ARF and ASF in the fluid, but the primary objective is to reduce the impact of ASF in order to enhance the effectiveness of ARF for microparticle manipulation. This objective is more easily attained by SSAW than by TSAW, as ASF generated by oppositely traveling TSAWs neutralize one another, thus reducing the overall strength of ASF. In addition, SSAW provides superior flexibility and operates at lower frequencies than TSAW[73].

Inside the microchannel, the surface standing acoustic wave produces a periodic pattern of pressure nodes (lowest pressure amplitude) and anti-nodes (highest pressure amplitude). Depending on the density, compressibility, and dimension of the microparticles and medium, the acoustic radiation force (ARF) induced by acoustic pressure drives the microparticle toward the

pressure nodes (PNs) or anti-nodes (PANs) in the SSAW region. It should be mentioned that based on the properties of the polystyrene microparticles used in this study, the acoustic radiation force on particles are towards the pressure nodes (PN) created inside the channel; in other words, particles will be focused on pressure nodes.

The movement of microparticles under the action of ARF in acoustofluidic devices in 1D harmonic standing waves (HSW) can be described by the ARF equation introduced by Yosioka and Kawasima's [74] are formulated as follows:

$$F_{rad} = -(\frac{\pi p_0^2 V_p \beta_f}{2\lambda_{SAW}})\phi(\beta,\rho)\sin(2kx) \quad \text{Eq. 2.2}$$

$$\phi(\beta,\rho) = \frac{5\rho_p - 2\rho_f}{2\rho_p + \rho_f} - \frac{\beta_p}{\beta_f} \quad \text{Eq. 2.3}$$

Where $V_p, p_0\ x, \beta, \lambda, \rho, k$ are the volume of the micro particles, acoustic pressure, distance from a pressure node, compressibility, wavelength, density, and wave number, respectively. The subscripts f and *p* represent the fluid and microparticle, respectively.

2.4 Governing equation for numerical simulations

In microfluidics, there are primarily two techniques to modelling the separation of particles and cells. The Lagrange method is the most popular technique for modeling the continuous separation of particles and cells. This method disregards Brownian motion and solves the Newtonian equation of single particle motion. Using an Eulerian approach, particles are treated collectively in terms of a time-dependent spatially variable concentration, which is determined using a partial differential equation that takes into account the drift force and Brownian diffusivity of the particles. The Euler method is typically utilized for nanoscale particle separation when Brownian motion effects are prominent. The Brownian forces are minimal due to the size of the

particles used in the majority of microfluidic separation research, which is typically hundreds of nanometers [75]. In this study, we therefore only consider the Lagrangian method, in which particles are modeled as discrete units, and each particle's motion is computed using classical Newtonian dynamics. Therefore, the numerical model acquired in this study is only suitable for Newtonian fluids such as water.

The particles' trajectory is computed by balancing the two major forces acting on them: acoustic radiation force (F_r) and fluid flow-induced drag force (F_D). The motion of the microparticle is calculated by Equation 2.4.

$$F_r + F_D = m_p \frac{du_p}{dt} \quad \text{Eq. 2.4}$$

where $m_p$and $u_p$are the mass and velocity of the particle, respectively, and t represents time. For spherical particles, the Gorchov [76] radiation force is described by Equations 2.5 and 2.6. Particle and fluid are represented by the subscripts *p* and *f*, respectively.

$$F_r = \nabla[V_p \left(\frac{3(\rho_p-\rho_f)}{2\rho_p+\rho_f} \overline{E_{kin}} - \left(1 - \frac{\rho_f c_f^2}{\rho_p c_p^2}\right) \overline{E_{pot}}\right)], \quad \text{Eq. 2.5}$$

where

$$\overline{E_{kin}} = \frac{1}{4}\rho_f |u_{ac}|^2, \overline{E_{pot}} = \frac{|p_{ac}|^2}{4\rho_f c_f^2} \quad \text{Eq. 2.6}$$

where V_p is the particle volume and ρ and c are the density and speed of sound, respectively. ($\overline{E_{kin}}$) and ($\overline{E_{pot}}$) represent the average kinematic and potential energy densities across time, respectively. The Stokes' drag force (shown in Eq. 2.4) was used to model the particles' drag force.

$$F_D = 3\pi\mu d_p(\langle v\rangle - v_p) \quad \text{Eq. 2.7}$$

where v is the average flow velocity throughout time. Furthermore, the distribution of harmonic acoustic pressure was computed using the Helmholtz wave equation [77], which is stated as follows:

$$\nabla.\left(-\frac{1}{\bar{\rho}_k}\nabla P\right) - \frac{\omega^2}{\bar{\rho}_k \bar{c}_k{}^2} P = 0, \quad \text{Eq. 2.8}$$

where P is the acoustic pressure and $\bar{\rho}_k, \bar{c}_k$, and ω are the equivalent medium density, corresponding medium sound velocity, and angular frequency, respectively.

The fluid flow simulation was done by solving the continuity and momentum equations.

$$\frac{\partial \rho}{\partial t} + \nabla.(\rho u) = 0, \quad \text{Eq. 2.9}$$

$$\rho\left(\frac{\partial u}{\partial t} + u.\nabla u\right) = -\nabla P + \mu\nabla^2 u + \left(\mu_b + \frac{1}{3}\mu\right).\mathrm{u} \quad \text{Eq. 2.10}$$

Where is ρ the fluid's density, P is its pressure, u is its flow velocity, and μ_b is its bulk viscosity.

The following are the linear piezoelectric constitutive equations:

$$\sigma_{ij} = C_{ijkl}s_{kl} - e_{ijm}E_m, \quad \text{Eq. 2.11}$$

$$D_m = e_{mij}s_{ij} + \varepsilon_{mk}E_k, \quad \text{Eq. 2.12}$$

Where σ is the matrix of mechanical stress and D is the electric displacement vector. The term E represents the electric field, $\varepsilon_{mk}$is the second-order tensor of the dielectric matrix, C_{ijkl} is the fourth-order elasticity tensor, e_{ijm} is the third-order piezoelectric stress matrix with the function of coupling the electric field with mechanical actuation, and s_{kl} is the second order strain tensor.

In this study the properties of material and operating conditions used in both our numerical and experimental studies are listed in Table 1[78].

Table 1) List of the properties of the material used in this study

Material	Symbol	Value
Water		
Density	ρ_0	997 $[kg/m^3]$
Speed of sound	c_0	1497 $[m/s]$
Shear viscosity	μ	890 $[Pa.s]$
Bulk viscosity	μ_b	2.47 $[mPa.s]$
PDMS		
Density	ρ_{PDMS}	920 $[kg/m^3]$
Speed of sound	c_{PDMS}	1076.5 $[m/s]$
Attenuation coefficient @ 6.65 MHz	α_{PDMS}	31 $[dB/cm]$
Polystyrene particle		
Density	ρ_{PS}	1060 $[kg/m^3]$
Speed of sound	c_{PS}	2050 $[m/s]$

2.5 Design of the two-stage acoustofluidic device

In this work, a two-stage parallel standing surface acoustic wave (paSSAW) acoustofluidic platform is designed to study the separation of microparticles. As demonstrated in Figure 2, the first stage of the device employs a combination of acoustic and hydrodynamic focusing mechanisms to boost the alignment efficiency prior to the second stage. The second module of the device separates the microparticles using a paSSAW acoustofluidics platform. At the focusing stage, the lateral location of the microchannel is shifted by $\lambda_{SAW}/4$ (with respect to the center of IDT distance) to have one pressure node at the channel's center. Moreover, two side sheath flows are applied to ensure that particles are in the area where the acoustic radiation force is towards the center.

At the separation stage, the microchannel is placed in the middle of the second pair of IDTs, which enables having one pressure anti-node at the center. Therefore, the focused particles entering this region will experience the acoustic radiation force toward the side walls. It should be mentioned that the location of PAN at this stage is slightly deviated from the focusing line

location (prior stage) to ignore symmetric particle migration.

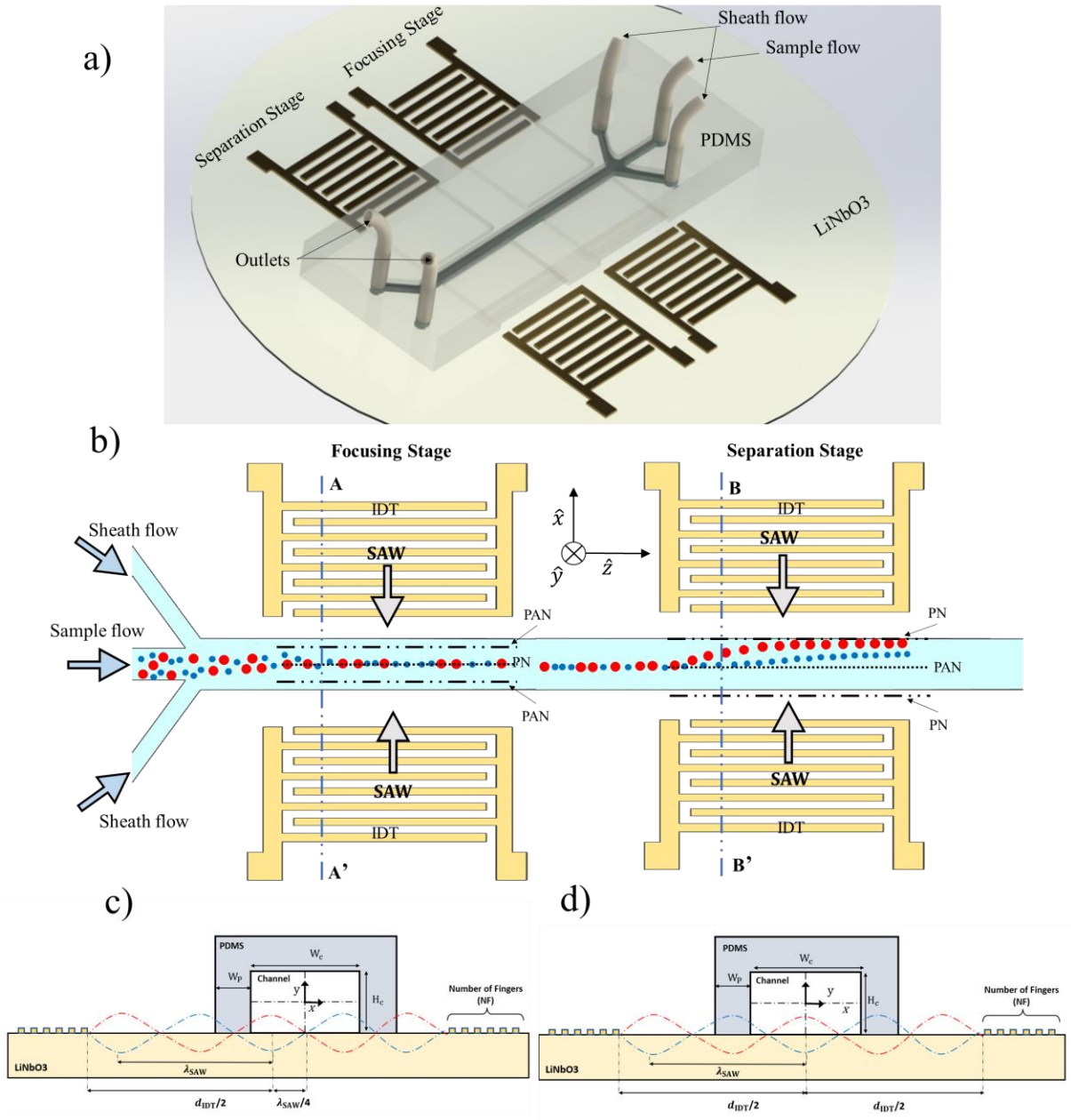

Figure 2) Schematic of the designed acoustofluidic device for microparticle separation. a) 3D SolidWorks model b) top view of the devise showing microparticle focusing at the first stage and separation at the second stage. c) cross section view of the focusing stage of the device (A-A') d) cross section view of the separation stage of the device (B-B')

Chapter 3: Experimental setup and microfabrication procedure

This chapter describes the microfabrication processes used to manufacture the acoustophoretic-based microparticle manipulator. Moreover, the experimental setup, instruments, and experimental procedures are detailed. The acoustophoretic-based device comprises interdigital transducers constructed of gold electrodes printed on a piezoelectric substrate and bonded to a polydimethylsiloxane (PDMS) channel. These components were fabricated using photolithography processes.

3.1 Fabrication of interdigital transducers

In this study, the designed interdigitated electrodes were fabricated using photolithography to create the pattern on gold-deposited piezoelectric substrates. We chose gold as the conducting layer due to its exceptional electrical conductivity and durability. Although, there is little bonding between gold and piezoelectric substrate. To improve adhesion, a thin layer of chromium is often placed on the substrate to provide sufficient bonding interaction between the gold and the substrate. For the fabrication of IDTs, first, a 15-nm layer of chromium followed by a 100-nm layer of gold was sputtered on the surface of the LiNbO3 wafer with a sputtering machine. Then, using a typical photolithography procedure, the electrodes were patterned. To do so, first, a thin layer of positive photoresist, S1805, was coated on the Lithium surface using a spin coater machine. Then, the coated substrate was soft-baked at 115 degrees Celsius on a hot plate for about one minute. Following that, using the mask aligner instrument, the substrate was exposed to UV light through a photolithography mask for about 10 seconds. Figure 3 shows examples of designed photomasks that were printed by CAD/Art Services, Inc. Following this step, the LiNbO3 wafer was submerged in a photoresist developer (MF-319 developer, MicroChem Corp.) to remove the unexposed photoresists. Next, through the wet etching process, gold and chromium etchants removed the

undesired gold and chromium, and the electrodes were subsequently patterned. Then, the residual photoresist was subsequently eliminated using a photoresist remover (MICROPOSIT® REMOVER1165). The chip was after that cleaned with DI water and dried with clean air. Figure 4 shows a LiNbO3 wafer through the fabrication process to pattern the IDTs.

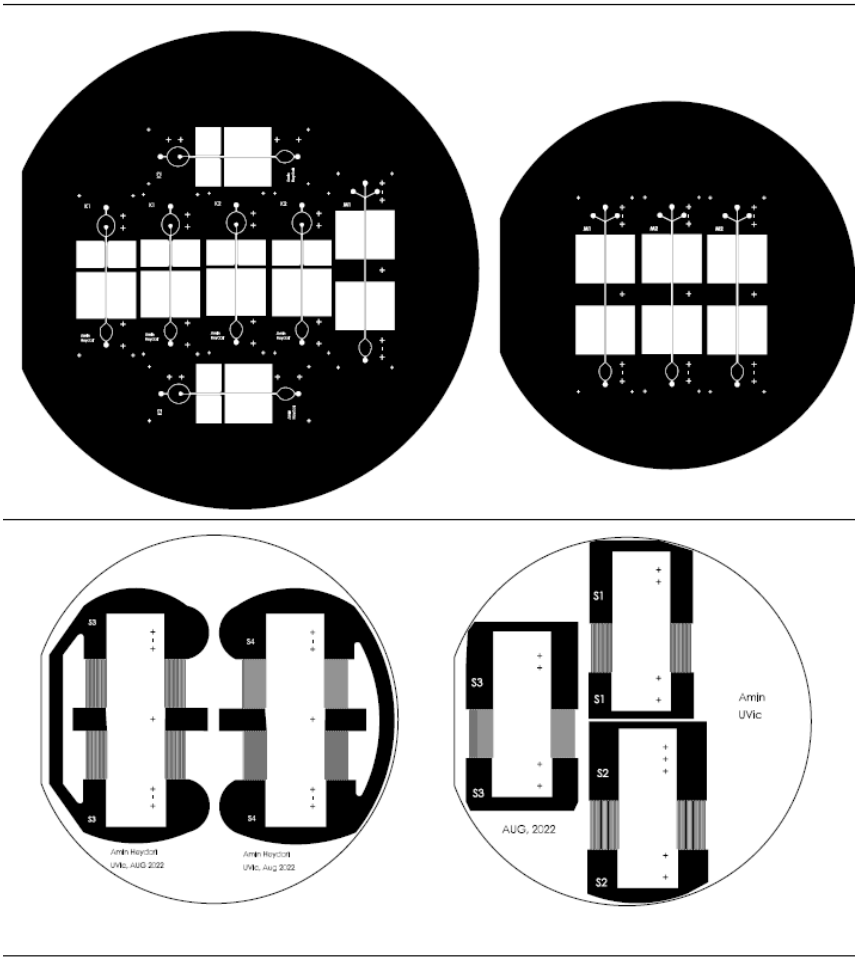

Figure 3) Photolithography masks printed by CADART for fabricating microchannels (top) and IDTs (bottom)

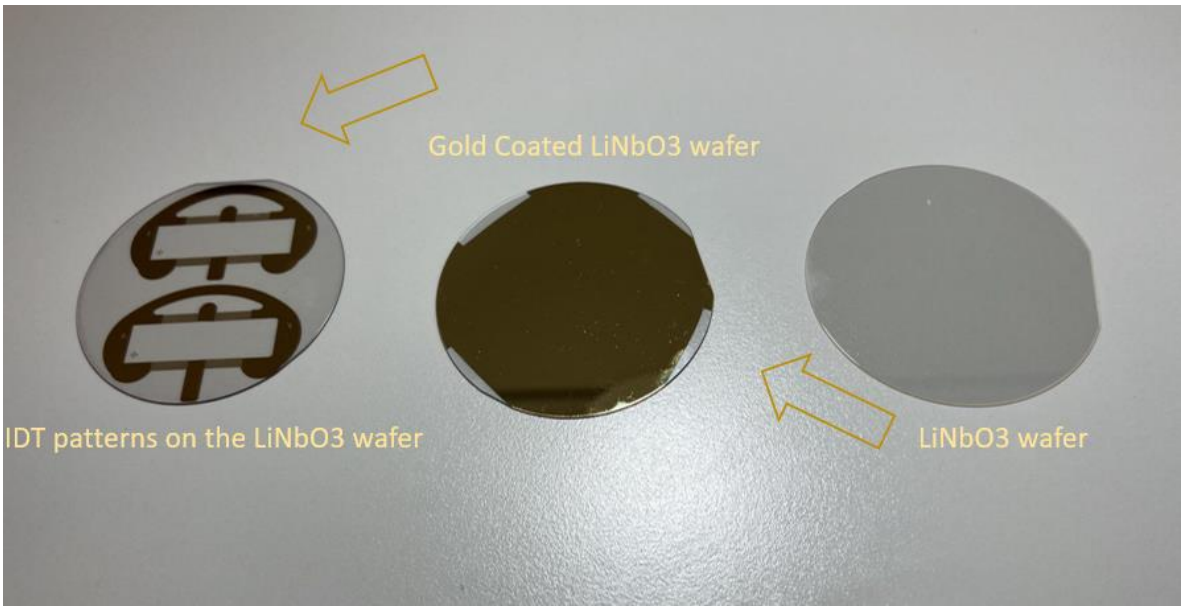

Figure 4) A LiNbO3 wafer through the fabrication process to pattern the IDTs

3.2 Microchannel fabrication

In order to create the PDMS-based microchannel, SU8 mold structures were created on silicon wafers. Then, using soft lithography, PDMS channels were fabricated from the molds. Depending on the designed height of the microchannel, the proper SU8 photoresist (either 2025 or 2075) was spin-coated on silicon wafers. Adjusting the proper coating speed, UV exposure time and baking times based on the information provided by the SU8 manufacturer (MicroChem) the desired height of the SU8 structure can be fabricated on the silicon substrates. After the spin coating of the photoresist was completed, the wafer underwent a soft-baking process at 65 degrees Celsius and then 95 degrees Celsius. The wafer was next subjected to ultraviolet radiation while it was placed in front of a custom-made photolithography mask. Figure 3 shows some examples of photomasks used for creating SU8 molds. During this step, the light was selectively transmitted through the portion of the mask that was transparent in order to crosslink SU8 with the desired

pattern on the chip. Following this step, there was a subsequent baking cycle at temperatures of 65 and 95 degrees Celsius. After that, the wafer was submerged in SU8 developer that was constantly being stirred while it was processing. Next, the wafer was cleaned with isopropanol and hard-baked at 150 degrees Celsius for half an hour. Furthermore, to form the PDMS channels in a weight ratio of 10 to 1, PDMS and its curing agent (SYLGARDTM 184 Silicone Elastomer, Dow Corning) were thoroughly combined and put into the created mold. After degassing the solution using a vacuum pump, the PDMS was put in an oven at 80-85 °C for about 4 hours to be cured.

3.3 Bonding PDMS to LiNbO3

After pealing the PDMS from its mold and cutting off the channels, the inlets and outlets were punched using a 1mm diameter Biopsy punch (Miltex R). Then, the channel and the IDTs were placed in an Oxygen Plasma machine to be plasma treated for 30 seconds and 1 minute, respectively. The power and the oxygen flow rate used for plasma treatment were 25 Sccm and 50 W, respectively. Finally, using a mask aligner instrument, the channel was precisely placed in its designed location on the substrate. Also, to establish a flawless bonding, the chip was heated at 80 degrees Celsius for 2 hours on a hotplate. Figure 5 represents an example of a fabricated acoustofluidic chip.

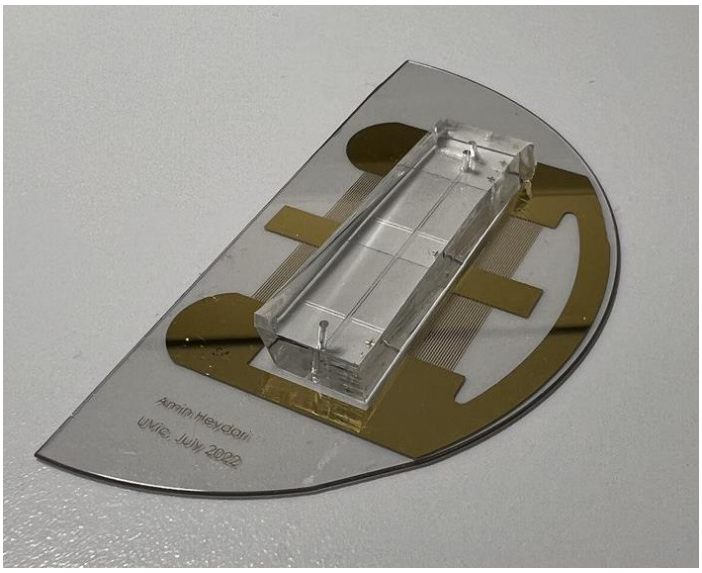

Figure 5) An example of an assembled two-stage acoustofluidic chip

3.4 Experimental setup and sample preparation Procedure

Figure 6 shows the experimental setup and other essential equipment used in this study. A KD-scientific syringe pump is used to pump particles and sheath flow through 1-mL, and 500 microL Hamilton gastight syringes into the micro-channel. A signal function generator ((81110A, Agilent Technologies Inc.)) and a power amplifier ((325LA, Electronics & Innovation Ltd)) are used to provide the appropriate RF signal with the desired frequency and amplitude to the IDTs. Using a microscope (Leica. upright microscope (Z16APO, Leica Microsystems GmbH) equipped with a DFC340FX camera), the trajectory of the particles is observed. v network analyzer (Figure 7) device (Nano VNA) was used. Consequently, after connecting the VNA to the chip using alligator connectors and sweeping over a range of frequencies around the expected one (see Eq. 2.1), the resonant frequency of each device was found.

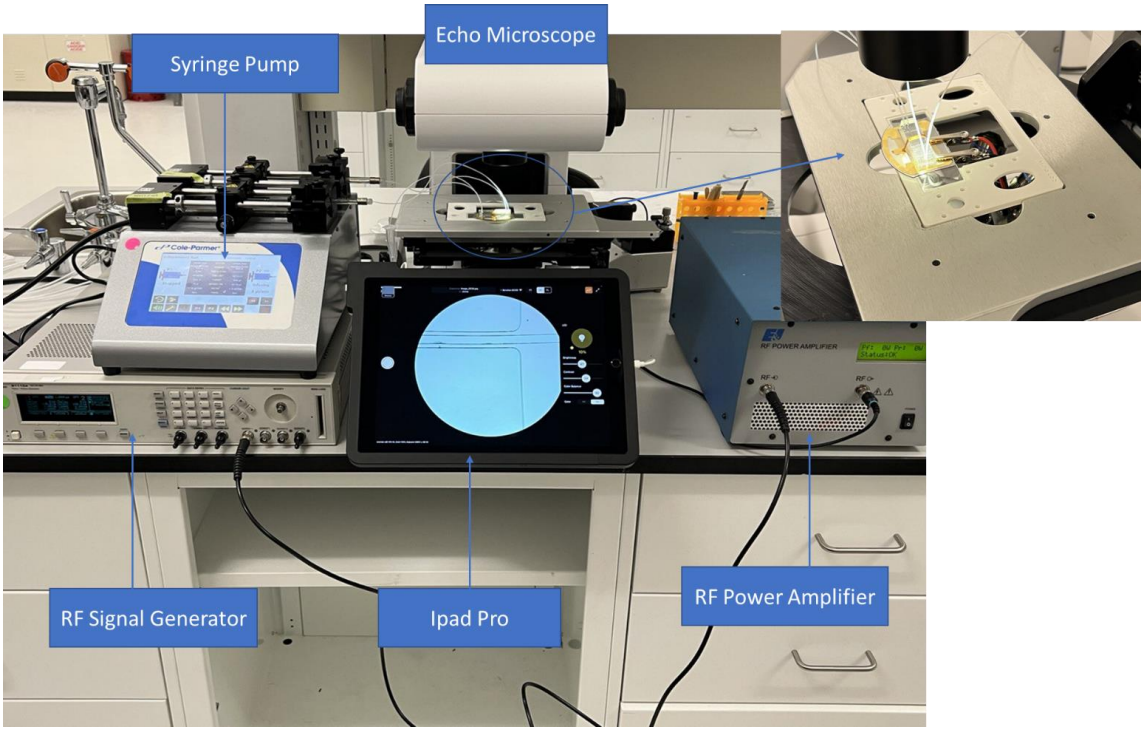

Figure 6) Experimental setup used in this study

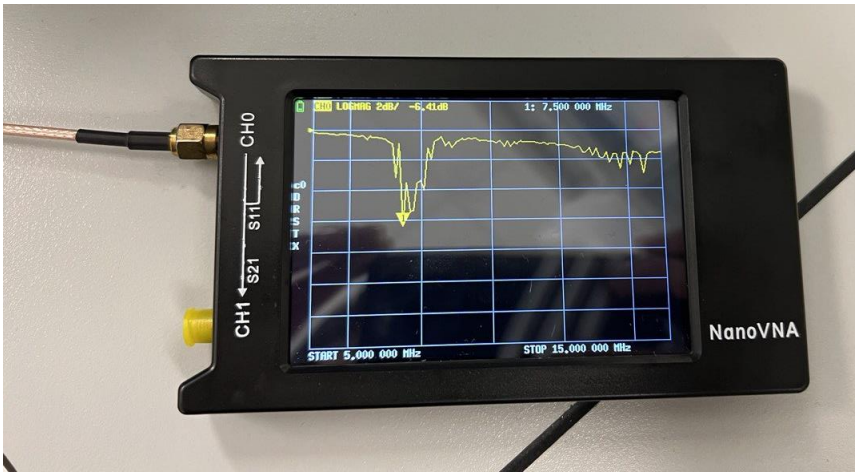

Figure 7) Using VNA device for measuring the resonance frequency of the fabricated IDTs

For sample preparation, different sizes of 5.0% *w/w* polystyrene (PS) microparticles (Phosphorex Inc.) with a concentration of 10 mg/ml were mixed in 1 mL aqueous solution.

Moreover, 0.1% *w/w* Tween-20 and 1.0% *w/w* Glycerol for lowering the PS microparticle adherence to microchannel walls and LiNbO3 surface were used as well.

Chapter 4: Results and Discussion

4.1 Investigating the effect of IDTs geometrical configurations

Many parameters, such as microchannel and IDT geometry, applied voltage, and flow rate, are involved in defining the performance efficiency of the acoustofluidic devices. Due to the IDT design's critical role in the SAW device's frequency response and, consequently, the maximum power transmission here, the IDT geometrical parameters, including the number of fingers (NF) and distance between IDTs (d_{IDT}) have been studied. First, a numerical study is performed to assess the influence of the number of IDT fingers and also the distance between electrodes (d_{IDT}). Before simulations, the mesh independency analysis was performed where maximum acoustic pressure inside the microchannel was calculated using different mesh elements. Here, the input parameters are the same as those defined in section 4.1.1. It was found that for the piezo area, a minimum mesh size of $\lambda_{saw}/8$, and for the PDMS/Fluid domain, a minimum mesh size of $\lambda_{saw}/25$ would provide acceptable precision (Figure 8-a). Moreover, Figure 8-b illustrates the structured mesh used for the numerical studies.

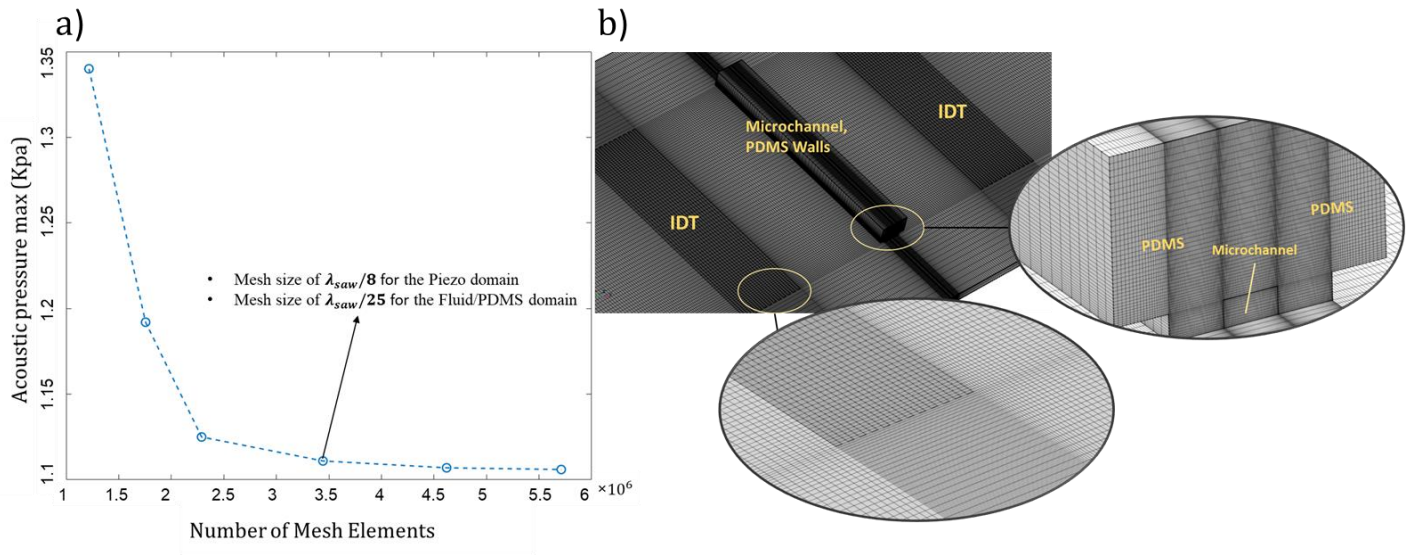

Figure 8) a) Mesh independency study, b) Illustration of the structured mesh used for the numerical studies

4.1.1 Numerical analysis of IDT features

The schematic of the simulation for this section is shown in Figure 9. Here, we use 2D numerical modeling to assess the influence of the number of fingers (NF) and IDT distance (d_{IDT}). For each IDT configuration, the maximum acoustic pressure at the center is calculated. Here, we use Eq. 2.1 to estimate the resonance frequency, it should be noted that this equation only provides an approximation, but the exact amount depends on many factors that may include any mismatch to the system. For each simulation in this section, the height and width of the microchannel, the width of the PDMS wall, and the SAW wavelength are as follows: H_C = 100μm , W_C = 200μm, $W_P = 100\mu m$ and λ_{SAW} = 400 μm. Also, the voltage applied is considered to be 2V.

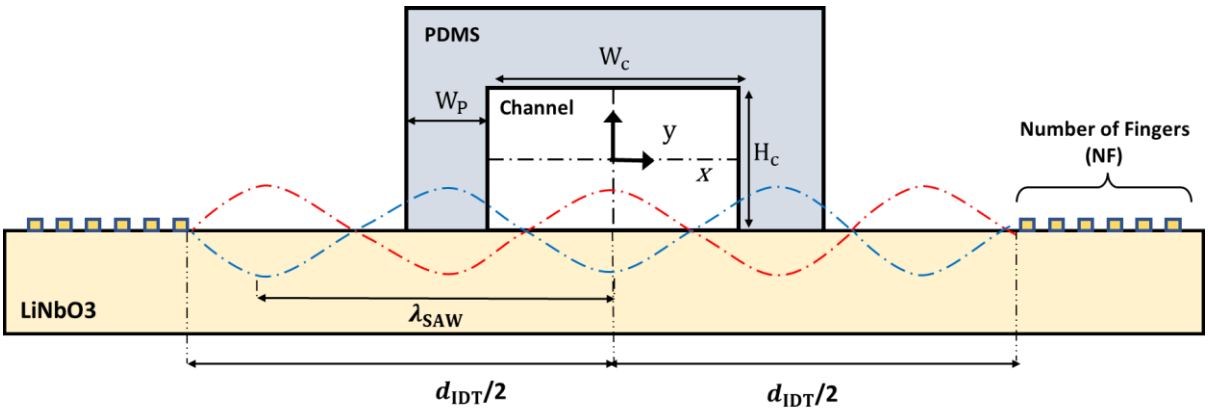

Figure 9) Schematic of the 2D numerical simulation for studying the effects of IDT configuration

First, the effect of the distance between IDTs was investigated. Figure 10 shows that besides the overall reduction in acoustic pressure by increasing the distance (due to the wave attenuation in the LiNbO3 substrate), locally, there is no specific pattern in maximum acoustic pressure variation vs. IDT distance. This indicates that for specific problems, different IDT distances would result in different acoustic pressure distributions; thus, investigating such parameters should be done for a specific design, preferably using experimental analysis.

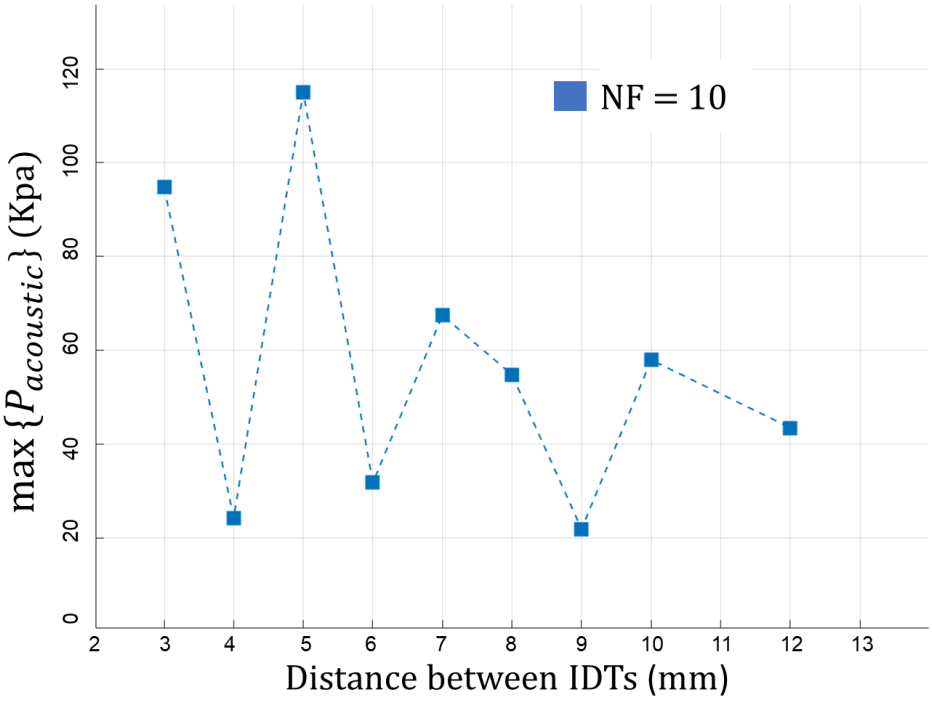

Figure 10) Variation of maximum acoustic pressure inside the channel based on different IDT distances, the number of IDT fingers NF = 10

The effect of the number of IDT fingers (NF) was then evaluated. As shown in Figure 11, NF = 10 and NF = 8 result in higher power transmission; after that NF = 12 and NF = 26 give a better result. Additionally, to ensure that the effect of the number of IDT fingers is not biased by the IDT distance, the effect of two different numbers of IDT fingers on the acoustic pressure for different IDT distances was compared. The results (Figure 12) show that for each number of IDT fingers, the same trend exists when changing the IDT distance meaning that the number of IDT fingers NF = 10 and NF = 8 would give better results in any IDT distance.

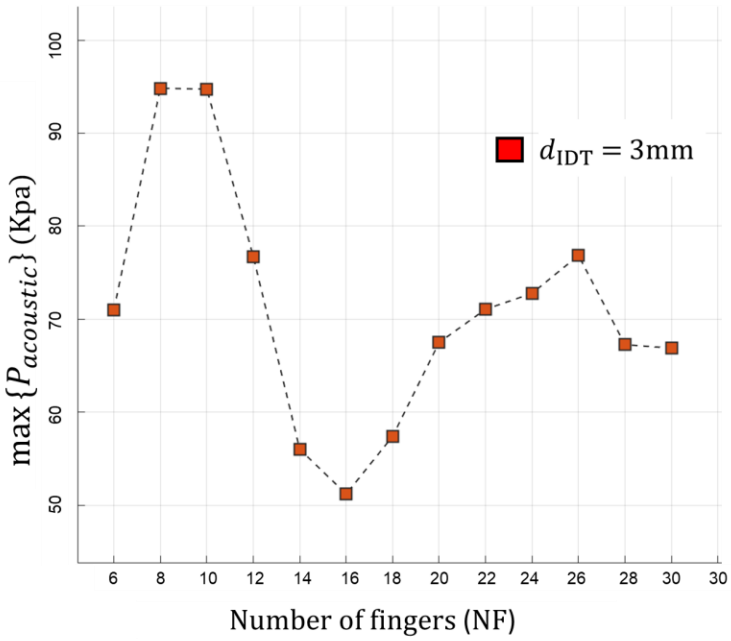

Figure 11) Variation of maximum acoustic pressure inside the channel vs. the number of IDT fingers where d_{IDT} = 3mm

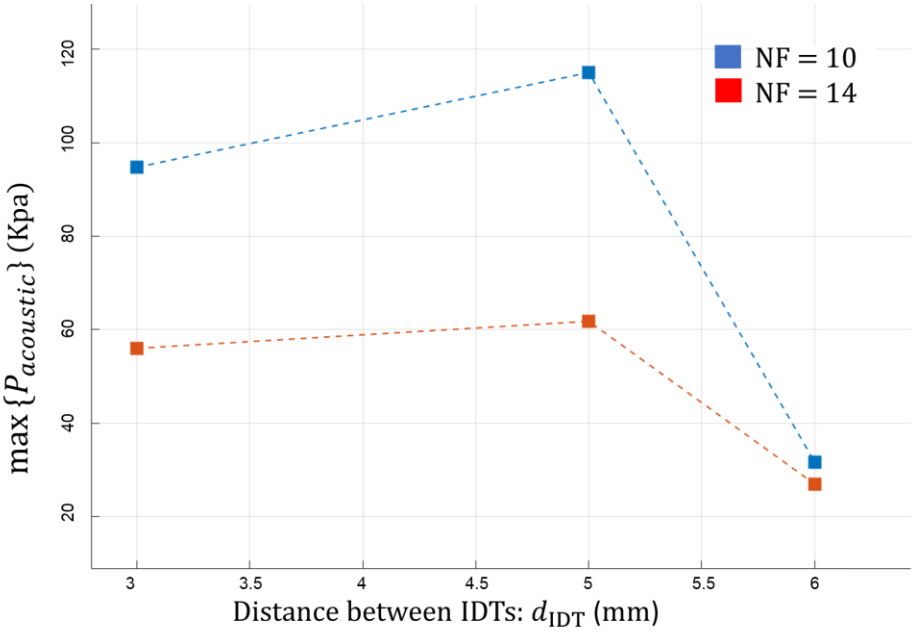

Figure 12) Comparing the effect of two different numbers of IDT fingers on the acoustic pressure for different IDT distances

4.2 Experimental analysis of IDT configuration

In this section, the IDT characteristic parameters, including the number of fingers (NF) and distance between electrodes, are experimentally investigated.

Two main critical parameters that drastically influence the performance and cover both electrical and mechanical characteristics of the acoustofluidic devices are the reflection coefficient (S11) and bandwidth. The acoustofluidic devices should be designed to show the minimum reflection coefficient (S11) [79] and maximum bandwidth for the effective isolation of particles from a wide size range (from sub-micron to micron) without significant heat and bubble generation. It is important to note that a SAW device's efficiency is frequently correlated with its quality factor, denoted by $QF = \frac{f_r}{\Delta f}$ (see Figure 13) where the width of the resonant peak in the frequency space is determined at half of the peak's greatest amplitude [80]. As the acoustofluidic devices work under radio frequency signals (RF), the RF generator and transmission line impedance should match the load for the highest power delivery. Any impedance mismatch between the source and load causes the signal to be reflected to the source.

In this section, we used VNA to obtain the frequency response of different IDT configurations. Figure 13 represents the RF frequency response of three different IDT models.

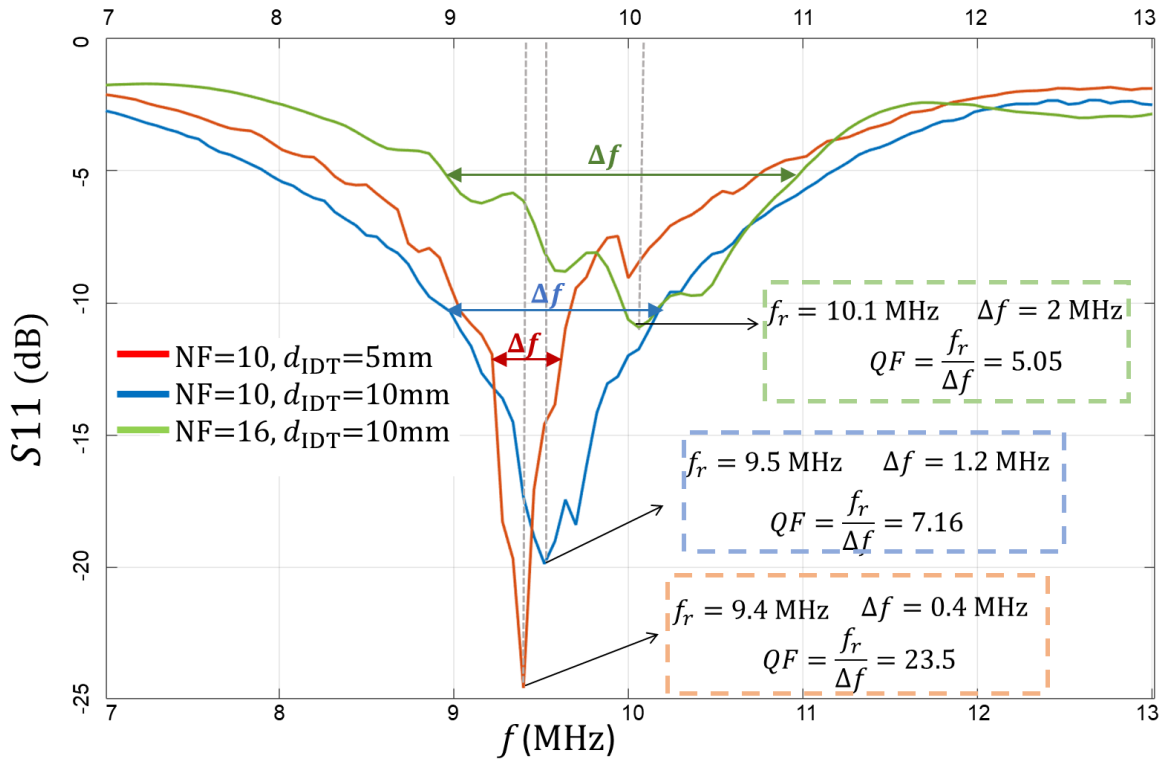

Figure 13) Reflection coefficient (S11) vs. frequency of three different IDT configurations measured using NanoVNA machine

Comparing two IDT designs, such as {NF = 10, and d_{IDT} = 5mm} with {NF = 16, and d_{IDT} = 10mm } shows that for the first design, the power transmission is high (most minor S11 parameter means the least reflection coefficient and highest power transmission)[79] but the quality factor (QF) is poor where any deviation from resonance frequency would significantly drop the power transmission. On the other hand, for the second design, the bandwidth is high (better QF), but the power transmission is weak. Lastly, for the third design IDT {NF = 10, and d_{IDT} = 10mm} the bandwidth and power transmission are balanced; therefore, for the rest of the experiments the designed IDTs feature 10 fingers with 10 mm distance between each two IDT pairs.

4.3 Numerical investigation of the effect of channel configurations, including PDMS walls

In this section, a 2D numerical analysis is performed to study the effect of channel features, including the PDMS wall thickness and channel aspect ratio, on the pressure distribution across the microchannel.

A numerical simulation is performed to show the morphology of wave propagation in the microchannel considering the acoustic window and PDMS wall thickness in the model. Two PDMS thicknesses of W_P=100µm and W_P=600µm is considered for a channel with a width of W_c=200µm and the height of H_c=100µm. The applied voltage is considered to be 2V. Also, for the rest of the simulations in this section, the height of the PDMS wall is H_P=600µm.

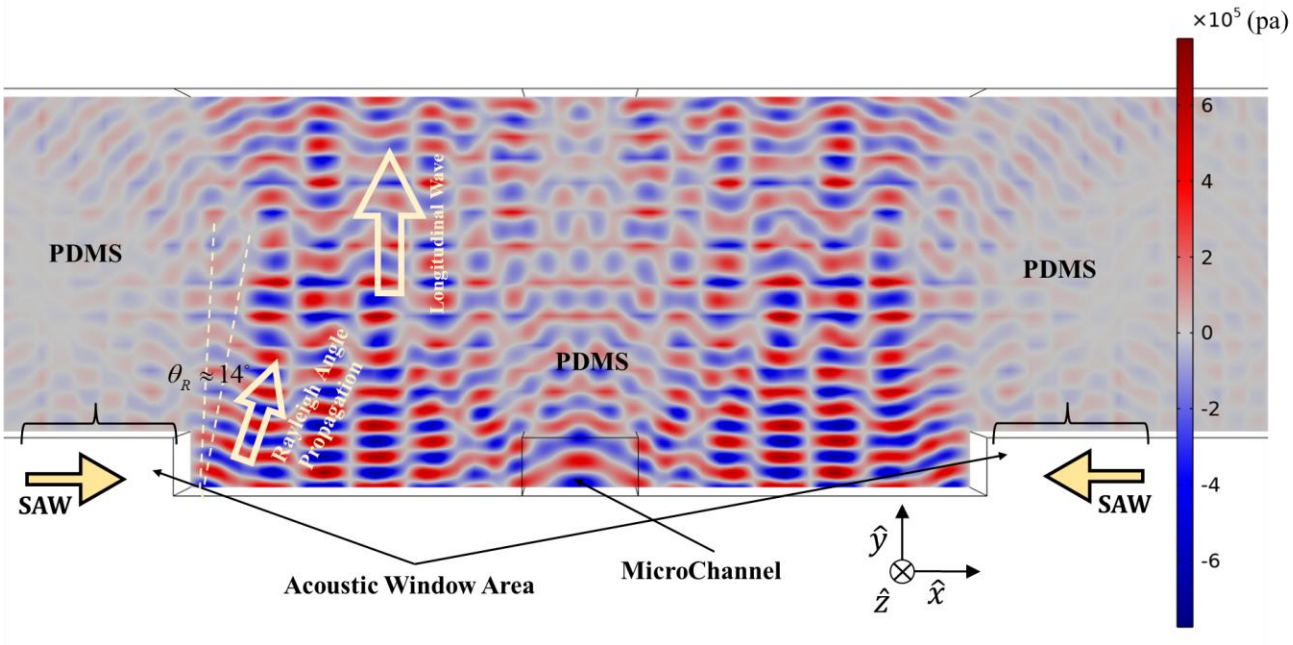

Figure 14) Contour of acoustic pressure distribution inside the PDMS wall and the microchannel ($W_P = 600\ \mu m,\ W_C = 200\ \mu m, H_C = 100\ \mu m\ \ \lambda_{SAW} = 200\mu m$)

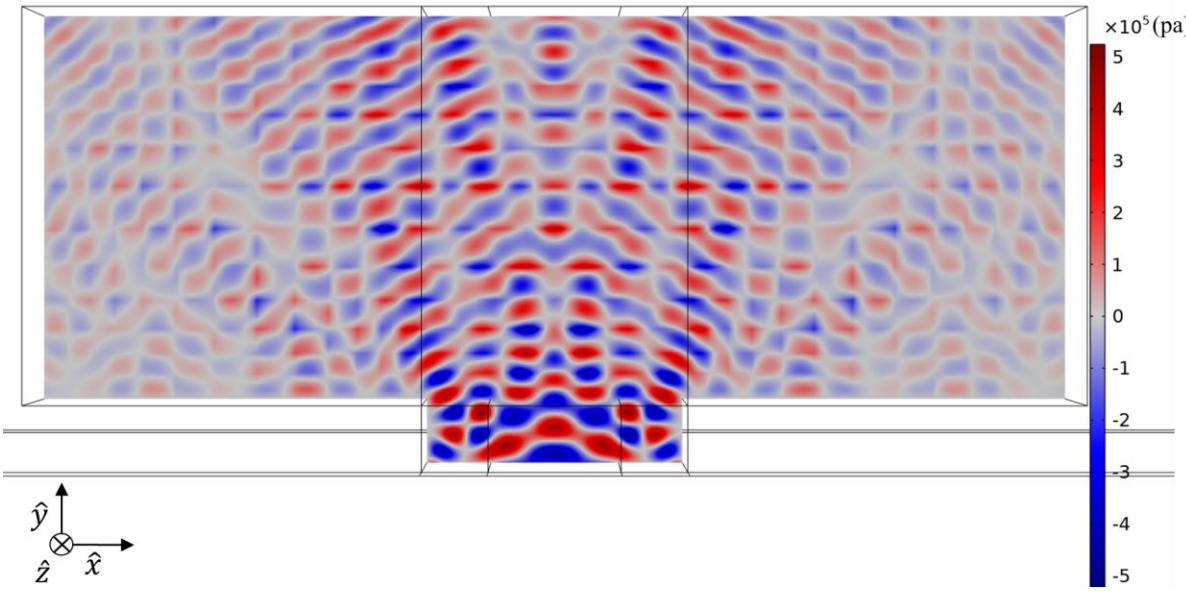

Figure 15) Contour of acoustic pressure distribution inside the PDMS wall and the Microchannel ($W_P = 100\ \mu m,\ W_C = 200\ \mu m, H_C = 100\ \mu m\ \ \lambda_{SAW} = 200\mu m$)

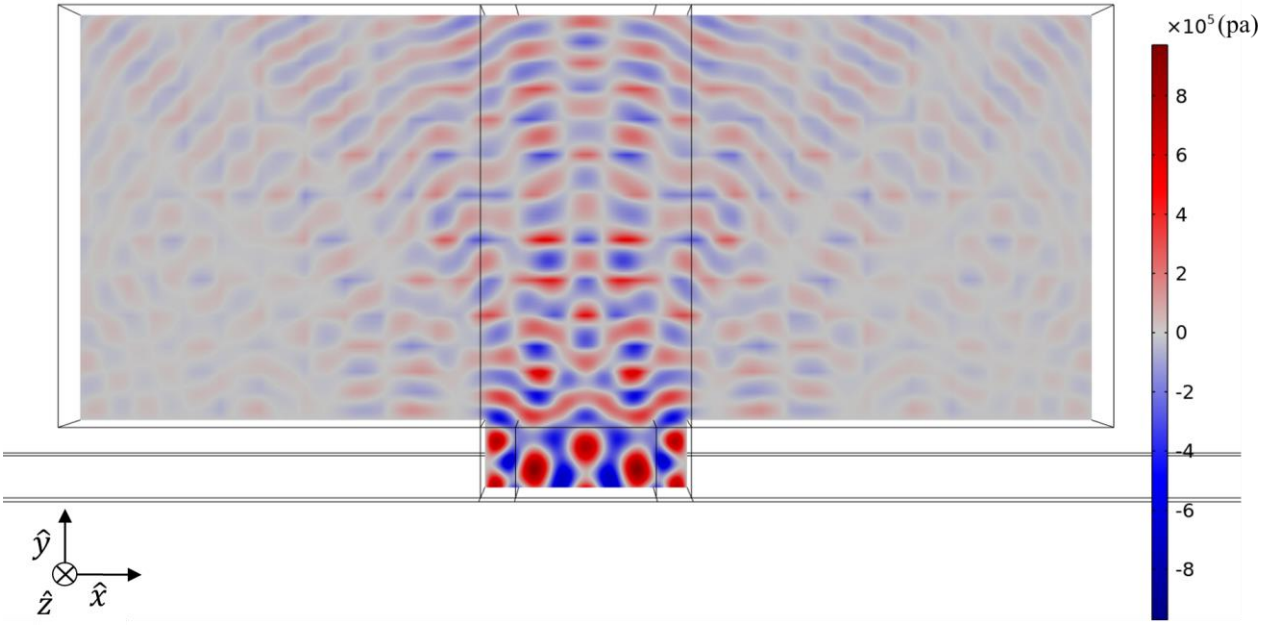

Figure 16) Contour of acoustic pressure distribution inside the PDMS wall and the Microchannel ($W_P = 50\ \mu m,\ W_C = 200\ \mu m, H_C = 100\ \mu m\ \ \lambda_{SAW} = 200\mu m$)

As it is demonstrated in Figure 14 - Figure 16, the SSAWs emit attenuating acoustic waves into the PDMS that propagate upward. In the PDMS, the refractive acoustic radiation changes immediately into longitudinal waves. At the contact between the PDMS and the LiNbO3, longitudinal waves propagate with a noticeable Rayleigh angle of 14, which is in accordance with Snell's law [81]. On the other hand, due to the mismatch between the acoustic impedance of the PDMS wall and water inside the channel, the incident wave is reflected at that interface. Although, given the short channel height, this reflection is counteracted by the leaky wave traveling from the PDMS wall to the center shortly after formation. Moreover, in the PDMS region, the weave propagation is primarily vertical, and a very weak wave propagation happens in the two PDMS regions above the acoustic window area. In the water region, though, a typical SSAW is formed, and it seems that the wave propagation has not been affected by the acoustic window. This is because the thickness of the PDMS wall is large enough (regarding the channel dimension and the wavelength of the SSAW). As the PDMS width reduces to $W_P = 100$ μm (Figure 15) and $W_P = 50$ μm (Figure 16), we can see that the regime of wave propagation changes drastically both in PDMS and water regions. Therefore, it can be concluded that depending on the channel dimension, PDMS width and the wavelength of the propagated SAW, different pressure distributions might happen inside the channel that can affect the microparticle manipulation. Furthermore, the maximum acoustic pressure inside the microchannels increases as the PDMS wall thickness decreases. Around $\sim 44\%$ and $\sim 63\%$ reduction in maximum pressure were observed when the PDMS thickness increased from 50 μm to 100 μm and 600 μm, respectively. To further investigate the effect of acoustic window configuration on the acoustic pressure distribution inside the channel, several simulations containing different dimensionless ratios, W_P/λ_{SAW}, W_C/λ_{SAW},

and H_C/λ_{SAW} are conducted. The contour of acoustic pressure distribution for each configuration is shown in Table 2.

Table 2) Acoustic pressure distribution contours and locations of pressure nodes (PN) for different SAW-channel configurations (Voltage = 2V for all cases)

Model Number	Acoustophoretic parameters	Acoustic Pressure Distribution
1	$\lambda_{SAW} = 400\ \mu m$ $W_C = 200\ \mu m$ $H_C = 50\ \mu m$ $W_P = 75\ \mu m$	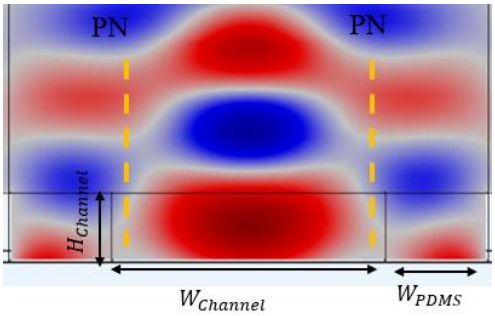
2	$\lambda_{SAW} = 400\ \mu m$ $W_C = 200\ \mu m$ $H_C = 50\ \mu m$ $W_P = 100\ \mu m$	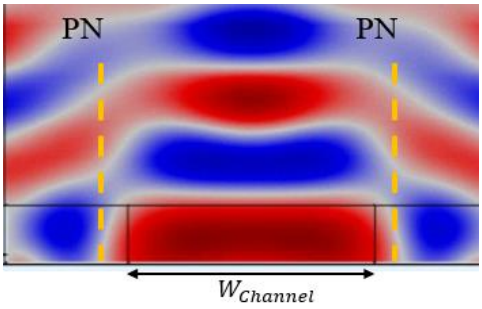

3	$\lambda_{SAW} = 400\ \mu m$ $W_C = 200\ \mu m$ $H_C = 50\ \mu m$ $W_P = 150\ \mu m$	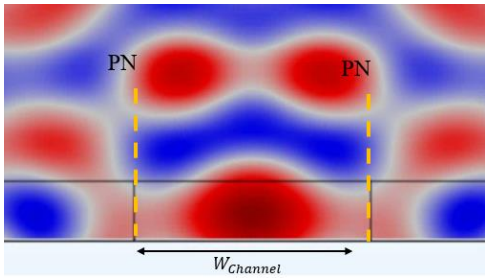
4	$\lambda_{SAW} = 400\ \mu m$ $W_C = 200\ \mu m$ $H_C = 50\ \mu m$ $W_P = 200\ \mu m$	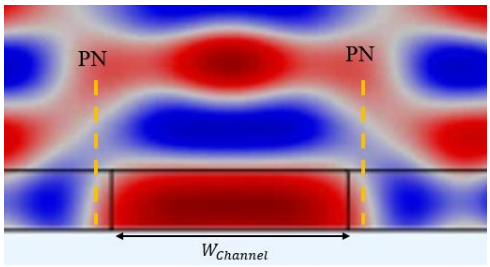
5	$\lambda_{SAW} = 400\ \mu m$ $W_C = 200\ \mu m$ $H_C = 50\ \mu m$ $W_P = 250\ \mu m$	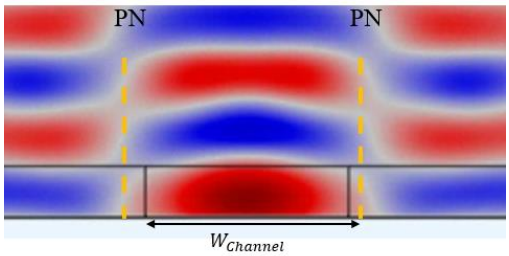

6	$\lambda_{SAW} = 400\ \mu m$ $W_C = 200\ \mu m$ $H_C = 100\ \mu m$ $W_P = 250\ \mu m$	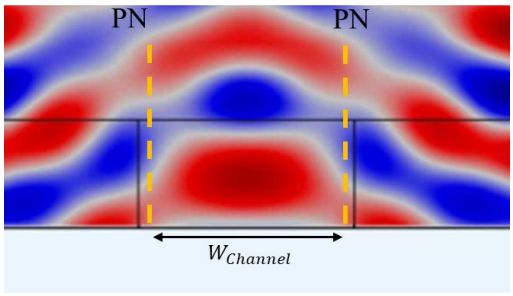
7	$\lambda_{SAW} = 400\ \mu m$ $W_C = 200\ \mu m$ $H_C = 100\ \mu m$ $W_P = 100\ \mu m$	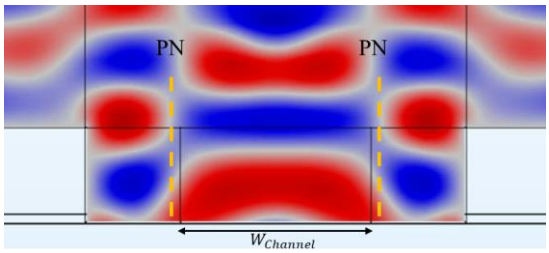
8	$\lambda_{SAW} = 300\ \mu m$ $W_C = 200\ \mu m$ $H_C = 50\ \mu m$ $W_P = 50\ \mu m$	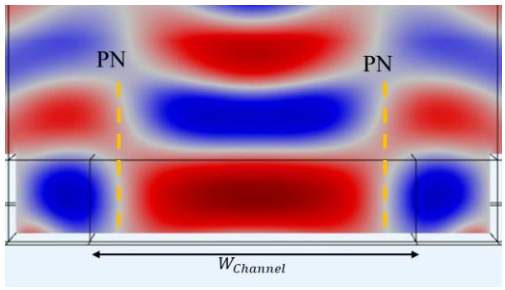

9	$\lambda_{SAW} = 300\ \mu m$ $W_C = 200\ \mu m$ $H_C = 50\ \mu m$ $W_P = 100\ \mu m$	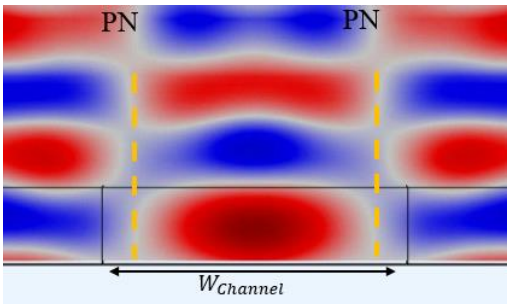

Considering the results provided in Table 2, it seems two parameters significantly affect the acoustic pressure distribution: the ratio of W_P/λ_{SAW} , and H_C/λ_{SAW}. For the small W_P/λ_{SAW} ratios the pressure distribution is completely affected by the acoustic window. On the other hand, for $W_P/\lambda_{SAW} > 0.5$ it seems the formation of waves is almost similar. It should be mentioned that the pressure distribution of model 5 remained constant as the PDMS wall thickness increased up to $W_P = 600\mu m$. On the other hand, the H_C/λ_{SAW} ratio also affects the pressure distribution. Comparing the results for model 5 and model 6 shows that for larger heights, when there is not enough PDMS/LiNbO3 interface for wave formation in the PDMS wall, the mismatch between acoustic impedances generates short wavelength acoustic waves around the top of the channel. Moreover, it should be mentioned that besides the PDMS wall thickness (W_P), channel aspect ratio W_C/H_C also shapes the pressure distribution and location of pressure nodes inside the channel. Shorter heights confine the wave within the walls of the channel, causing smoother pressure distribution across the channel width, whereas for higher channel heights, the formed pressure distribution is sharp.

Similarly, the acoustic pressure distribution is obtained for the particle focusing module where the channel was shifted by $\lambda_{SAW}/4$ from the center of the IDT pair. Figure 17 represents

the pressure distribution for one of the configurations studied ($W_P = 100\ \mu m,\ W_C = 200,\ H_C = 100\ \mu m,\ \lambda_{SAW} = 400\ \mu m$). As can be seen, although $W_C = \lambda_{SAW}/2$ yet due to effect of the PDMS wall, the two pressure anti-node (PAN) that were expected to be on the channels wall are located inside the channel. This contraction in the wavelength due to PDMS wall effect was observed for all the cases studied (even for cases where the width of the channel was smaller than the half of the wavelength ($W_c < \lambda_{SAW}/2$).

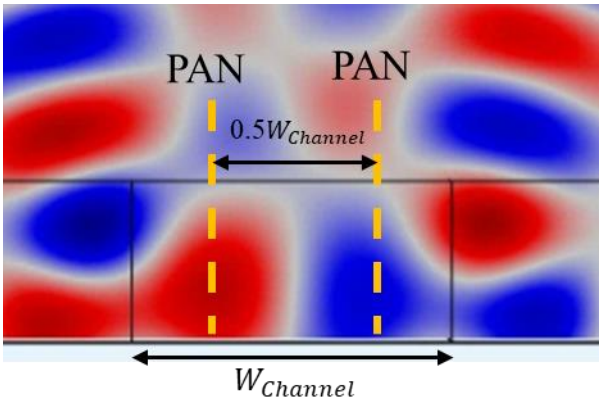

Figure 17) Pressure distribution and the location of pressure anti nodes (PANs) inside the microchannel in the focusing mode ($W_P = 100\ \mu m,\ W_C = 200\ \mu m, H_C = 100\ \mu m\ \ \lambda_{SAW} = 400 \mu m$).

This observation reveals the importance of using side sheath flow to assist the acoustic focusing module, by pre-focusing the particles within the desired acoustic field region (where the acoustic radiation force is toward the channel's center) and preventing particle aggregation towards the channel walls.

4.4 Sensitivity Analysis

In this part, a sensitivity analysis is performed to assess the numerical model prediction of acoustic pressure distribution inside the. Here, for the analysis of a single factor the sensitivity S is defined by Eq 4.1:

$$S = \Delta K/\Delta X \qquad \text{Eq. 4.1}$$

where ΔX and ΔK are the differences in the parameters and the results (distance between two PANs), respectively. Comparing the sensitivity values in table three indicates that the variation in the width of the channel has the highest impact on the location of PANs, where increasing the channel length by 5mm leads to the deviation in the distance between PANs by 6 mm. Overall, the sensitivity values in Table 3 demonstrate that the validation of the numerical model will not be affected by common fabrication errors.

Table 3) Sensitivity analysis study of the predicted acoustic pressure distribution, where X represents the parameters, and K denotes the distance between PANs (Figure 17)

Parameter, X	**Parameter variation, ΔX**	**Parameter variation (%) 100×ΔX/X**	**Result, K**	**Result variation, ΔK**	**Result variation (%) 100×ΔK/K**	**Sensitivity, S**
$W_{Channel}$=200µm	5 µm	2.5%	99 µm	2.18 µm	2.2%	0.436
$H_{Channel}$=100µm	5 µm	5%	99 µm	1.09 µm	1.1%	0.29
W_{PDMS}=100µm	5 µm	5%	99 µm	3.96 µm	4%	0.79
λ_{SAW}=400µm	5 µm	1.25%	99 µm	0.1 µm	0.1 %	0.02

4.5 Numerical study of particle manipulation in the focusing stage

Here, we use the COMSOL particle tracing module, which closely resembles experimental particle tracing and velocimetry, to examine the acoustophoretic motion of particles inside the microchannel. This module gives a Lagrange explanation of the motion of the particles where the location of each microparticle is individually assessed at various time intervals.

In this section, the particle focusing stage of the device is numerically simulated to investigate the effects of several parameters, such as sample flow rate, sheath flow rate, applied voltage, and size of microparticles, on the performance of the focusing stage. The 3D model of this simulation was created using COMSOL modeling software (Figure 18). The parameters used for the next simulation are shown in Table 4.

Table 4) Input value of the parameters used for the particle focusing simulation

Parameter	**Value**
IDT number of fingers (NF)	10
Distance between IDTs (d_{IDT})	5 cm
Channel length	15 mm
Channel width (W_C)	200 μm
Channel height (H_C)	50 μm
Wavelength (λ_{SAW})	400 μm
PDMS thickness (W_P)	200 μm

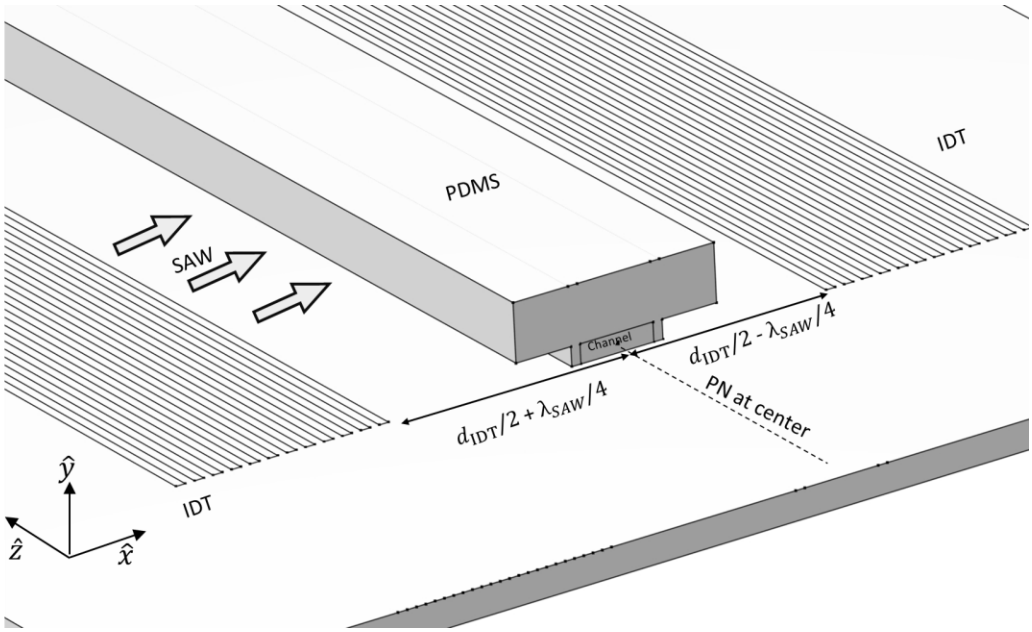

Figure 18) 3D model of the particle focusing stage (the model does not show the exact dimension)

For the following simulations, particles are released at different locations respecting the channel center. According to the results obtained in the previous part (Figure 17), the distance between two anti-pressure nodes inside the microchannel was obtained to be $\sim 50\%$ of the channel width; thus, to avoid particle aggregation on the side walls in each simulation, the sheath flow rate needs to be at least equal to the sample flow rate ($\dot{Q}_{Sheath} = \dot{Q}_{sample}$).

In order to study the effect of microparticle size on the focusing performance, eight particles with the diameters of D = {2µm, 3µm, 4µm, 5µm, 6µm} are released at the pressure anti node on the left side of the channel. The applied voltage and the sample flow rate are 2V and 0.02 µl/min, respectively. As shown in Figure 19, larger particles focus much faster toward the centerline. This is due to the fact that the acoustic radiation force is related to the volume of particles, as indicated in Eq. 2.5.

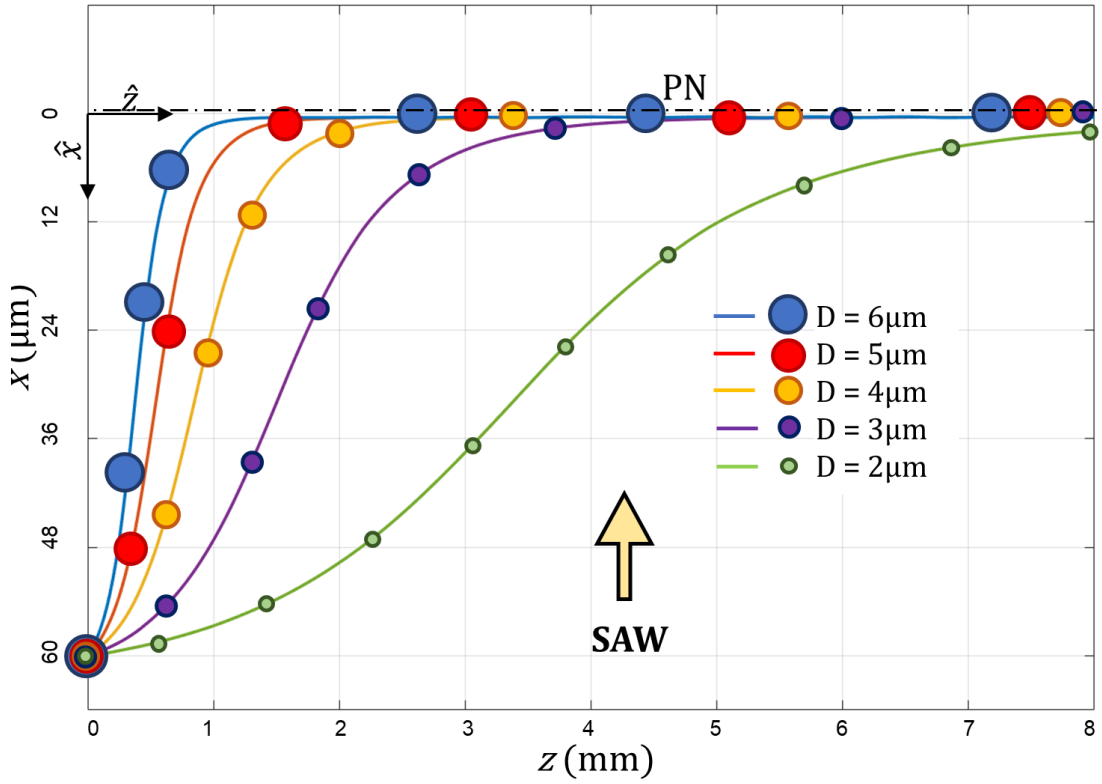

Figure 19) Microparticle focusing trajectory for different sizes (x and z denote the channel's width and length directions, respectively).

Figure 20 demonstrates the lateral component of acoustic radiation force ($F_{r,x}$) on different particles along their migration toward the pressure node. The radiation force on each particle is zero at the pressure nodes and anti-nodes. At the pressure anti-node, the gradient of pressure is zero, whereas at the pressure node, the zero acoustic pressure results in zero acoustic radiation force. It should be mentioned that the direction of acoustic radiation force is inward at the pressure node while its direction is outward on the pressure anti-node, indicating that any misalignment in the location of particles relative to pressure anti-nodes could cause an entirely different displacement path for particles; Therefore, in real applications, it is crucial to make sure that the sheath flow rate is high enough to focus all of the particles towards the center line. Additionally, as indicated in Figure 20, the maximum lateral acoustic force exposed on the particle with a

diameter of 6 µm ($\left|F_{r,x}\right| \approx 2.5 pN$) is almost eight times the force exposed on the particle with a diameter of 3µm ($\left|F_{r,x}\right| \approx 0.31 pN$), which is in accordance with Eq. 2.4.

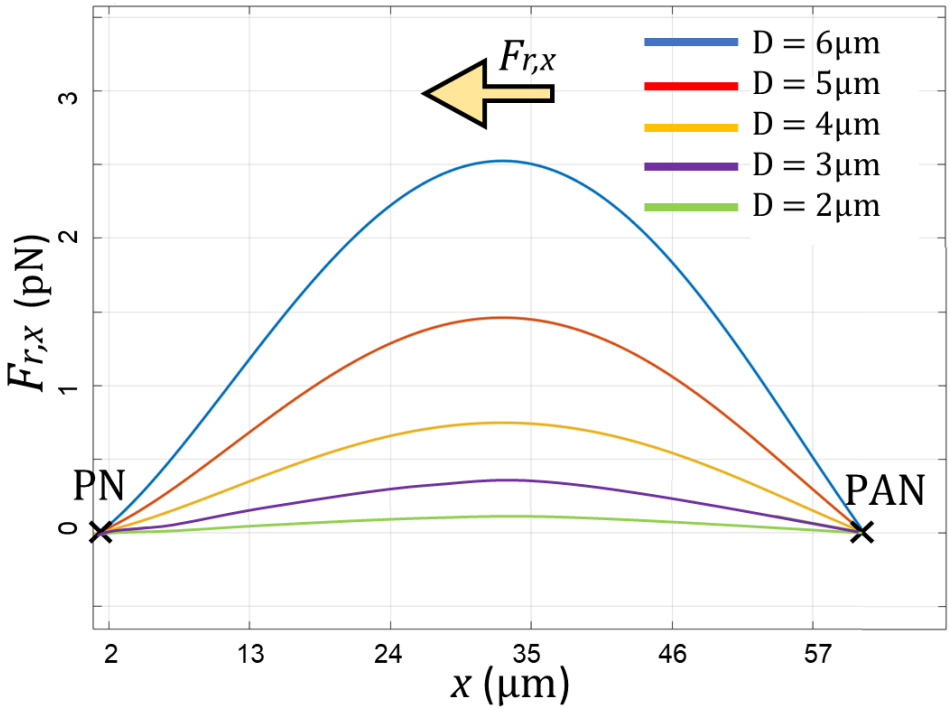

Figure 20) Lateral component (x direction) of the acoustic radiation force on particles with diameters of 2, 3, 4, 5, and 6µm during their displacement towards the center of the channel, Voltage=2V

Estimating the minimum channel length required for achieving the desired focusing efficiency is one of the main factors in designing the focusing stage. It should be mentioned that longer channels increase the chances of particle degradation and adhesion to the walls, cost of fabrication, and energy loss. Knowing this, the optimum design should provide maximum efficiency at the shortest channel length possible. This entirely depends on the application the device is used for, which means that the size of particles to be focused, the desired flow rate, and

the available power source determine the minimum channel length that must be provided. Figure 21 and Figure 22 show the results of particle tracing for two particles with diameters of 6 µm and 4 µm, where the minimum channel length needed for focusing at different flow rates and voltages are compared.

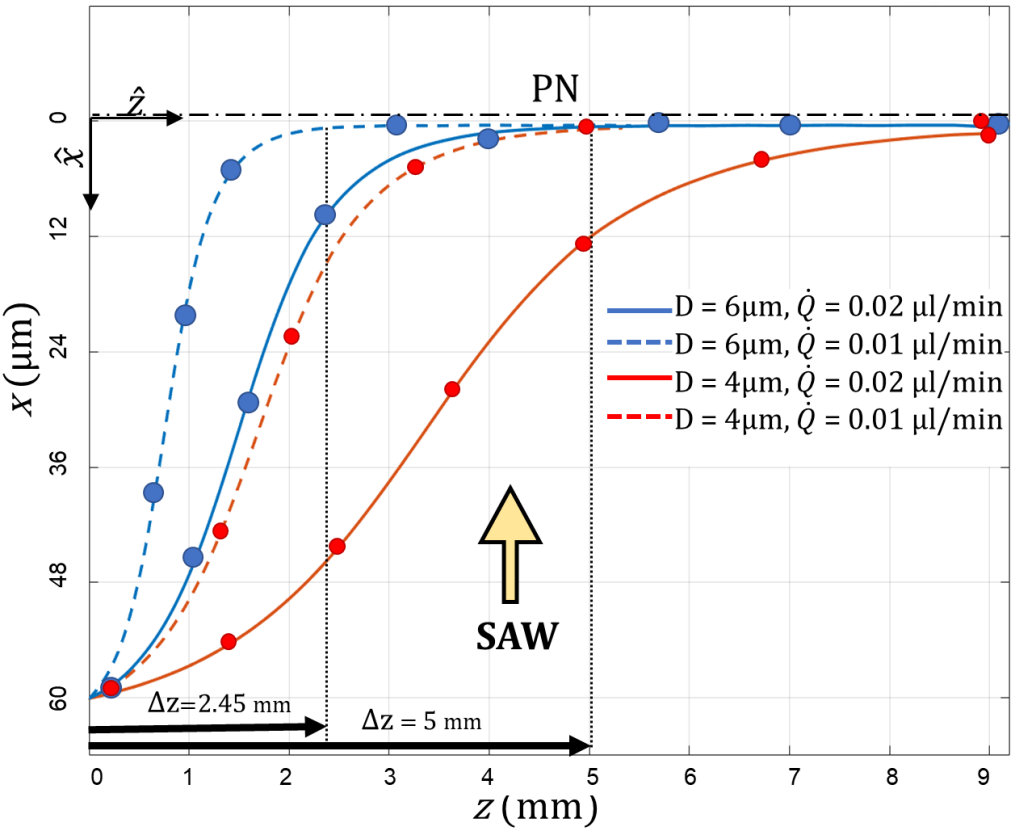

Figure 21) Microparticle focusing trajectory at different sample flow rates, Voltage=2V

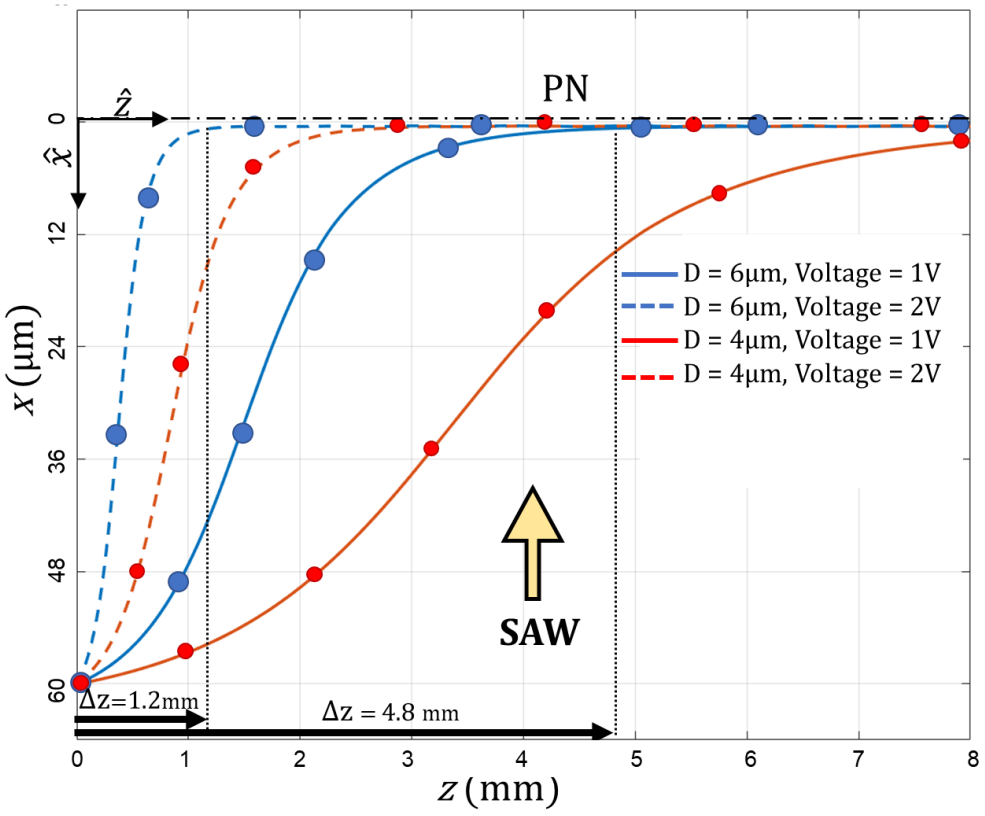

Figure 22) Microparticle focusing trajectory at different Voltages, and $\dot{Q}_{sample} = 0.64\mu l/min$

As it is represented in Figure 21, the focusing length increases from 2.45mm to 5mm ($D_P = 6\mu m$) when the sample flow rate increases from $\dot{Q}_{sample} = 0.01\mu l/min$ to $\dot{Q}_{sample} = 0.02\mu l/min$ respectively. This specifies that the required focusing length and the flow rate are directly related. This is due to the fact that the drag and acoustic radian forces applied on the particles are perpendicular to the flow direction; subsequently, higher flow rates dictate longer channel lengths to realize the desired focusing thickness. In Figure 22, the required focusing length for the particles with the diameters of $4\mu m$ and $6\mu m$ at two different applied voltages (1V and 2V) are compared. The results show that doubling the applied voltage reduces the minimum length four times for each particle. As it is indicated in Eq. 2.2 the radiation force is directly proportional

to the square of input power (applied voltage). Therefore, doubling the voltage would create four times stronger acoustic force resulting in four times higher acceleration for each particle which reduces the traveling time to half according to the basic equations of motions. It should also be mentioned that the drag force is the direct reaction of acoustic force as other forces are supposed to be small enough to be neglected (Eq. 2.4). Therefore, higher acoustic force would result in higher drag force on particles.

In Figure 23, the time variation of the lateral component of drag and acoustic radiation forces exposed on two microparticles with the diameters of ($D = 4\mu m$, and $D = 6\mu m$) across the microchannel widths (from one PN to the center PAN) are compared. For both particles, the ratio of the maximum acoustic force to the drag force remains constant when increasing the applied voltage from 1V to 2V. Therefore, it can be concluded that increasing the applied voltages will increase both drag and acoustic radiation forces in the same manner. However, it should be mentioned that in cases where acoustic streaming happens inside the channel, the acoustic radiation force is not equal to the drag force.

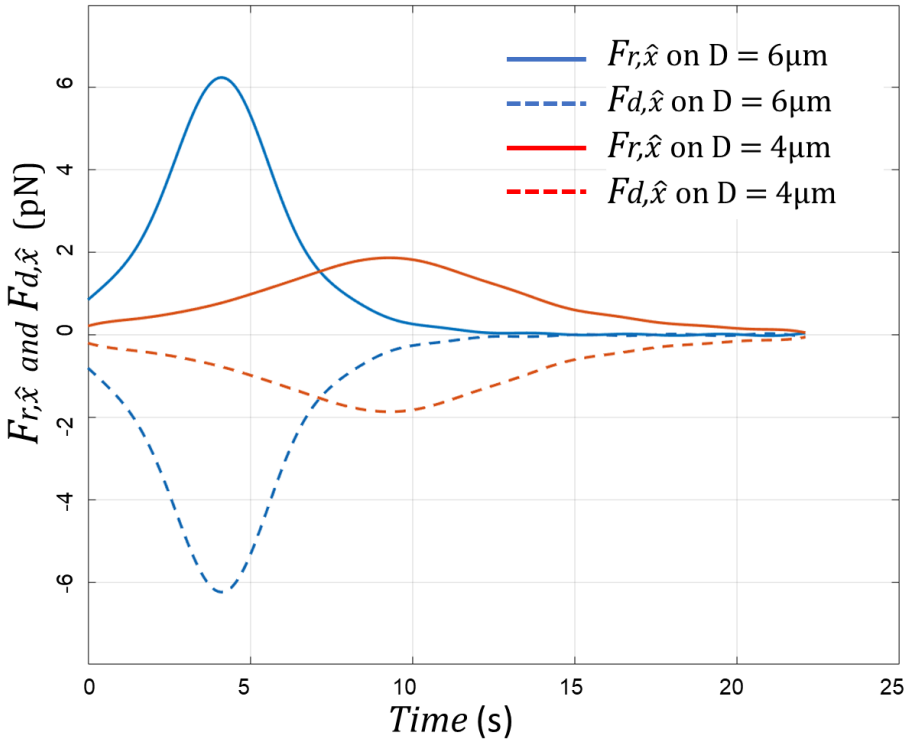

Figure 23) The time variation of lateral component of drag and acoustic radiation forces exposed on two microparticles with different sizes

As was previously discussed, the acoustic pressure inside the channel has a 2D distribution resulting in the variation of acoustic radiation force at different heights and widths of the channel. For example, Figure 24 represents the pressure distribution across the channel's widths at different heights. Higher pressure amplitude at the middle height reduces to lower pressure amplitude near the top of the channel. Therefore, to better assess the focusing performance of the device in the next simulation, particles are released at different locations with respect to the pressure anti-nodes (PANs).

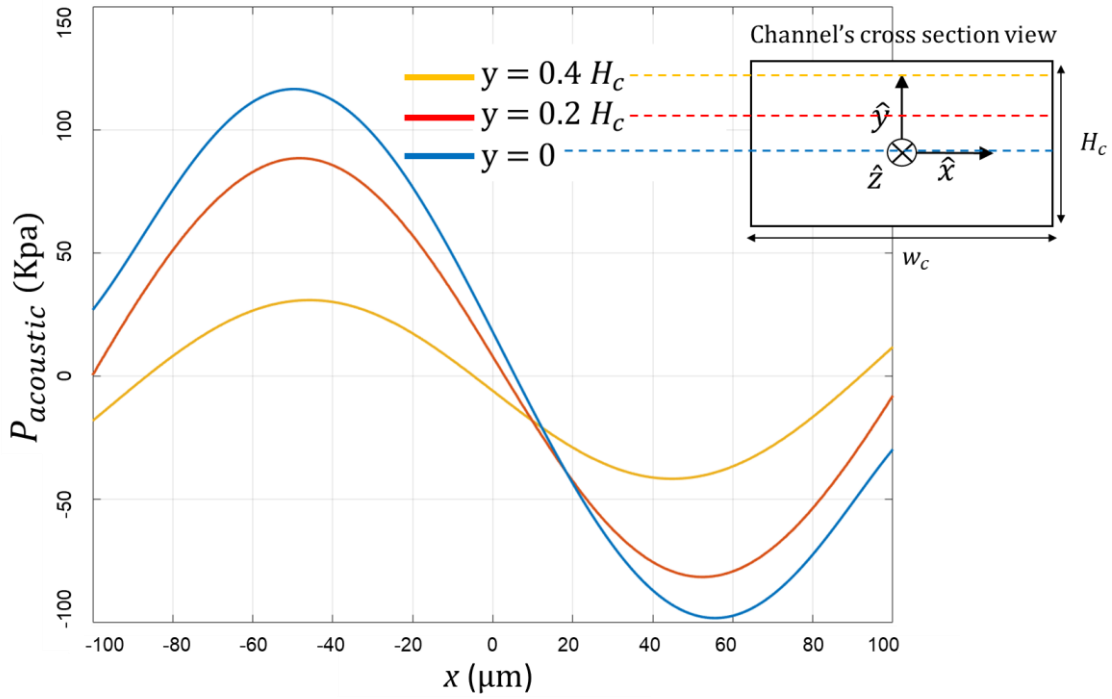

Figure 24) Acoustic pressure distribution across the channel's width in different heights for the case study defined in Table 4 and Voltage =2V.

In the next simulation, $4\mu m$ diameter particles are released from different heights (between $y = 0$ and $y = 0.4H_{Channel}$). The sample flow rate and the voltages are $0.02\mu l/\text{min}$ and 2V, respectively. As shown in Figure 25, for each particle, the focusing thickness is increasing as depending on the initial locations of particles, the acoustic radiation force derives them in different paths towards the channel centerline where the pressure node is located. In addition to the variation of the acoustic radiation force, the velocity of particles is also different at various heights. Therefore, not every particle with the same size would have the same final distance from the pressure nodes, and some particles will not even reach the outlets and stick to the walls instead, as the acoustic force applied to them are towards the channel walls than the channel center. In the end, depending on the application, to boost the focusing efficiency, proper channel length must be acquired to have the minimum focusing thickness possible.

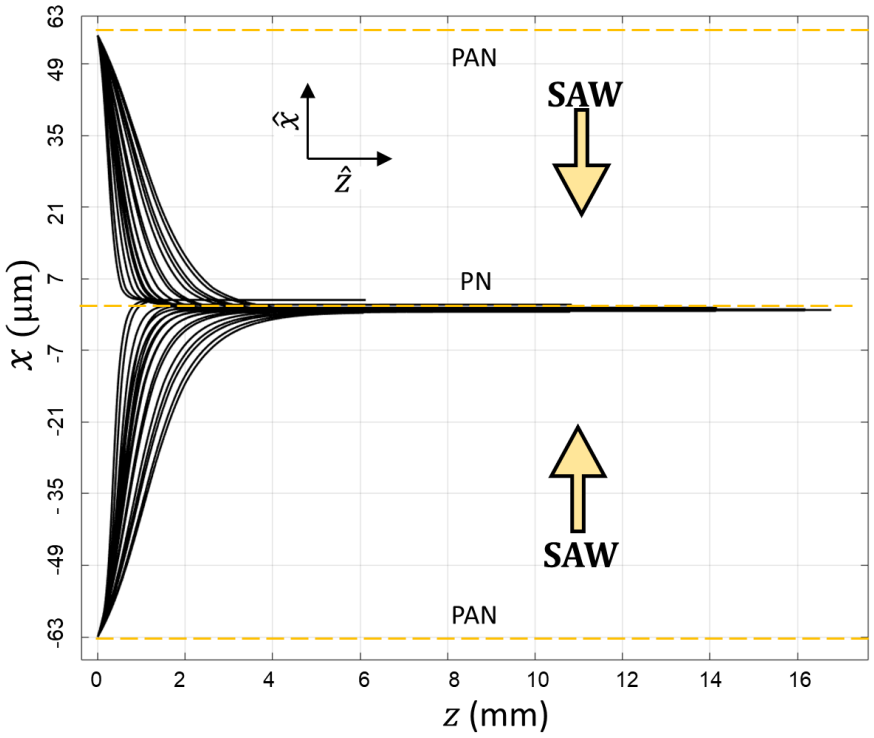

Figure 25) Focusing thickness for 4μm diameter microparticles released from different heights.

Earlier, we observed that in conventional $W_c = \lambda_{SAW}/2$ channel-IDT designs for flow focusing the pressure anti-nodes are not located on the side walls necessarily; thus, a sheath flow must be acquired to confine the particles in the area where the acoustic force is towards the center.

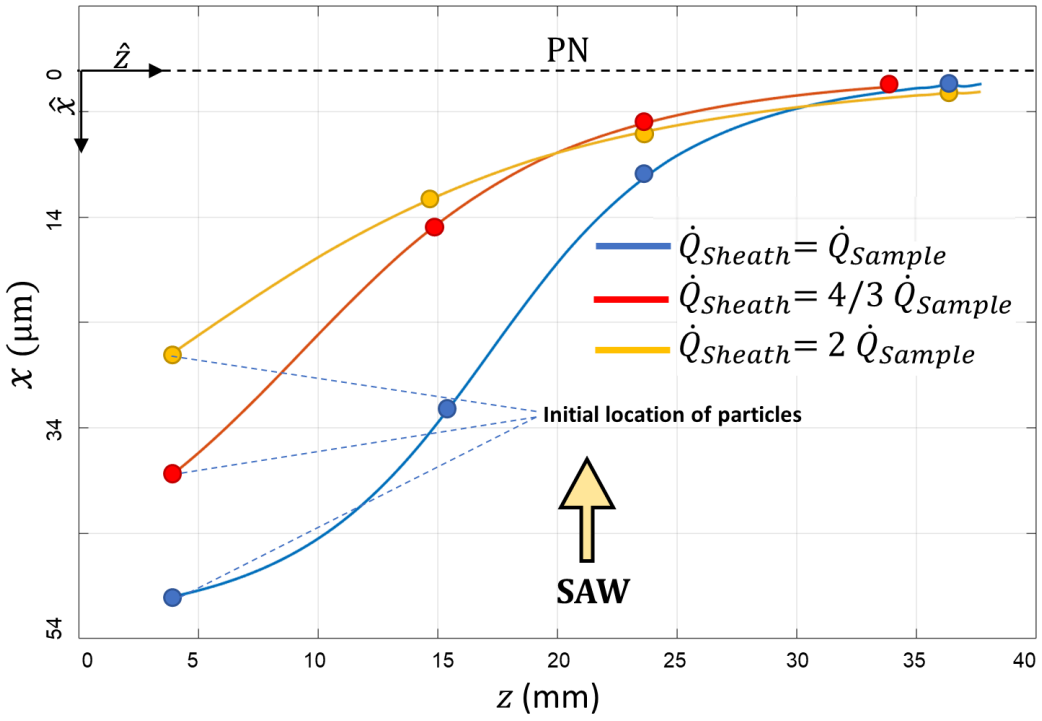

Figure 26) 2μm diameter microparticle focusing using different sheath flow rates (voltage = 2V and $\dot{Q}_{sample}$=0.016μl/min).

To study the effect of sheath flow rate on the focusing performance. The particle trajectory of 2μm diameter microparticles under different sheath flow rates ($\dot{Q}_{Sheath} = \dot{Q}_{sample}$, $\dot{Q}_{Sheath} = 4/3\dot{Q}_{sample}$, and $\dot{Q}_{Sheath} = 2\dot{Q}_{sample}$) is simulated. The results shown in Figure 26 indicate that increasing the sheath flow rate to $4/3\dot{Q}_{sample}$ and $2\dot{Q}_{sample}$ decreases the initial distance of the particle from the pressure node (channels center) to approximately about 75% and 50%, respectively. Up to about 16mm from the starting point along the channel length the $\dot{Q}_{Sheath}$=$2\dot{Q}_{sample}$ condition seems to have better focusing thickness. After that point, the $\dot{Q}_{Sheath}$=$4/3\dot{Q}_{sample}$ case starts to result in better focusing thickness. Finally, at the end of the channel $\dot{Q}_{Sheath} = 2\dot{Q}_{sample}$ case leads to the poorest focusing thickness compared to other ratios.

We observed that from half of the channel toward the end $\dot{Q}_{Sheath} = 4/3\dot{Q}_{sample}$ case leads to the best focusing thickness. Therefore, we can conclude that for a given channel length, depending on the acoustic pressure distribution, applied voltage, and sample flow rate, there is an optimum sheath flow rate to have a more efficient focusing performance. To better understand the reason behind this phenomenon, the acoustic radiation forces on particles are represented in Figure 27. As can be seen for the condition when the sheath flow rate is equal to $\dot{Q}_{sample}$ the starting point of particles is far away from the location where particles receive the maximum acoustic radiation force. Besides particles in $\dot{Q}_{Sheath} = 2\dot{Q}_{sample}$ condition never experienced the maximum acoustic force. However, in the case of $\dot{Q}_{Sheath} = 4/3\dot{Q}_{sample}$ the majority of the particle migration toward the center is within the maximum acoustic radiation force area. Thus, the focusing performance is more efficient.

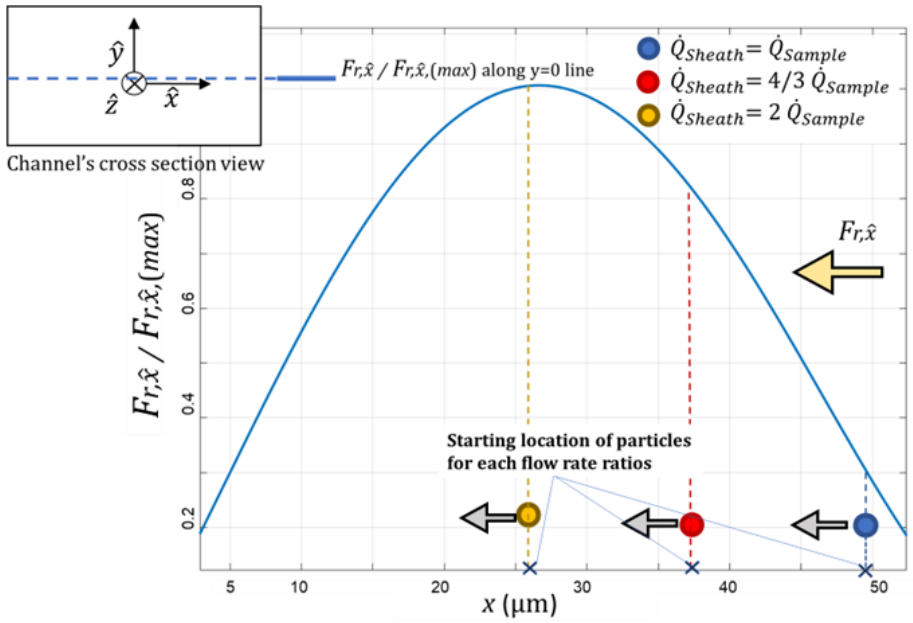

Figure 27) Normalized acoustic radiation force experienced by 2μm diameter particles at different lateral locations based on different sheath flow rate ratios (voltage = 2V and $\dot{Q}_{sample}$=0.016μl/min).

4.6 Numerical simulation of the separation stage

In this part, numerical simulations are performed to study the performance of the separation module of the device. Three combinations of channel geometry and wavelength are indicated in Table 5 will be assessed to investigate the effect of the pressure distribution across the channel length on the separation efficiency. The separation stage of the device is modeled as a microchannel located at the middle of a pair of IDTs and the particles are released from the center of the channel inlet. Three sets of microparticles D= $\{2\mu m$, and $1\mu m\}$, D = $\{4\mu m$, and $6\mu m\}$, and also D = $\{10\mu m$, and $12\mu m\}$will be used for this part to assess the binary separation for each device configuration. The particle sets are considered to cover a wide range of sizes and diameter ratios. The separation performance will be assessed based on the lateral distance (width direction) that separates two particles(Δd_x) along the channel length.

Table 5) Configuration parameters of the devices used for simulating the separation performance

Design	**Number of fingers (NF)**	**IDT Distance**	$\boldsymbol{\lambda_{SAW}}$	$\boldsymbol{W_C}$	$\boldsymbol{H_C}$	$\boldsymbol{W_P}$
I	10	5mm	$400\mu m$	$200\mu m$	$100\mu m$	$200\mu m$
II	10	5mm	$300\mu m$	$200\mu m$	$50\mu m$	$250\mu m$
III	10	5mm	$400\mu m$	$200\mu m$	$50\mu m$	$100\mu m$

In this section, first, a numerical study is performed to clarify the effect of the size and the size ratio of particles on the separation performance. Three sets of microparticles: **i**: D = $\{2\mu m$, and $1\mu m\}$ with the geometric mean size of 1.4 μm and the size ratio of r_D = 2, **ii**: D = $\{4\mu m$, and $6\mu m\}$ with the mean size of 4.9 μm and the size ratio of r_D = 1.5, and **iii**: D = $\{10\mu m$, and $12\mu m\}$ with the mean size of $11\mu m$ and the size ratio of r_D = 1.2 were separated considering the Design

I channel configuration. As it is shown in Figure **28**, separating $\{10\mu m$ and $12\mu m\}$ with the mean size of $11\mu m$ can be performed at the highest flow rate (0.32 µL/min) whereas much less flowrate (0.016 µL/min) must be acquired in case of separating $\{1\ \mu m$ and $2\ \mu m\}$ with the mean size of 1.4 μm. This shows that for a limited channel length and power supply the higher the sizes of particles are the more the throughput can be achieved in separation. Moreover, the maximum separation distance in separating $\{1\mu m$, and $2\mu m\}$with the size ratio of r_D = 2 is Δd_x= 86 μm which is 10% and 78% more than the maximum separation distance of separating $\{4\mu m$, and $6\mu m\}$ with r_D = 1.5 and $\{10\mu m$,and $12\mu m\}$ with r_D = 1.2 respectively. This indicates that the higher the size ratio is the higher the maximum separation distance can be achieved in separating microparticles.

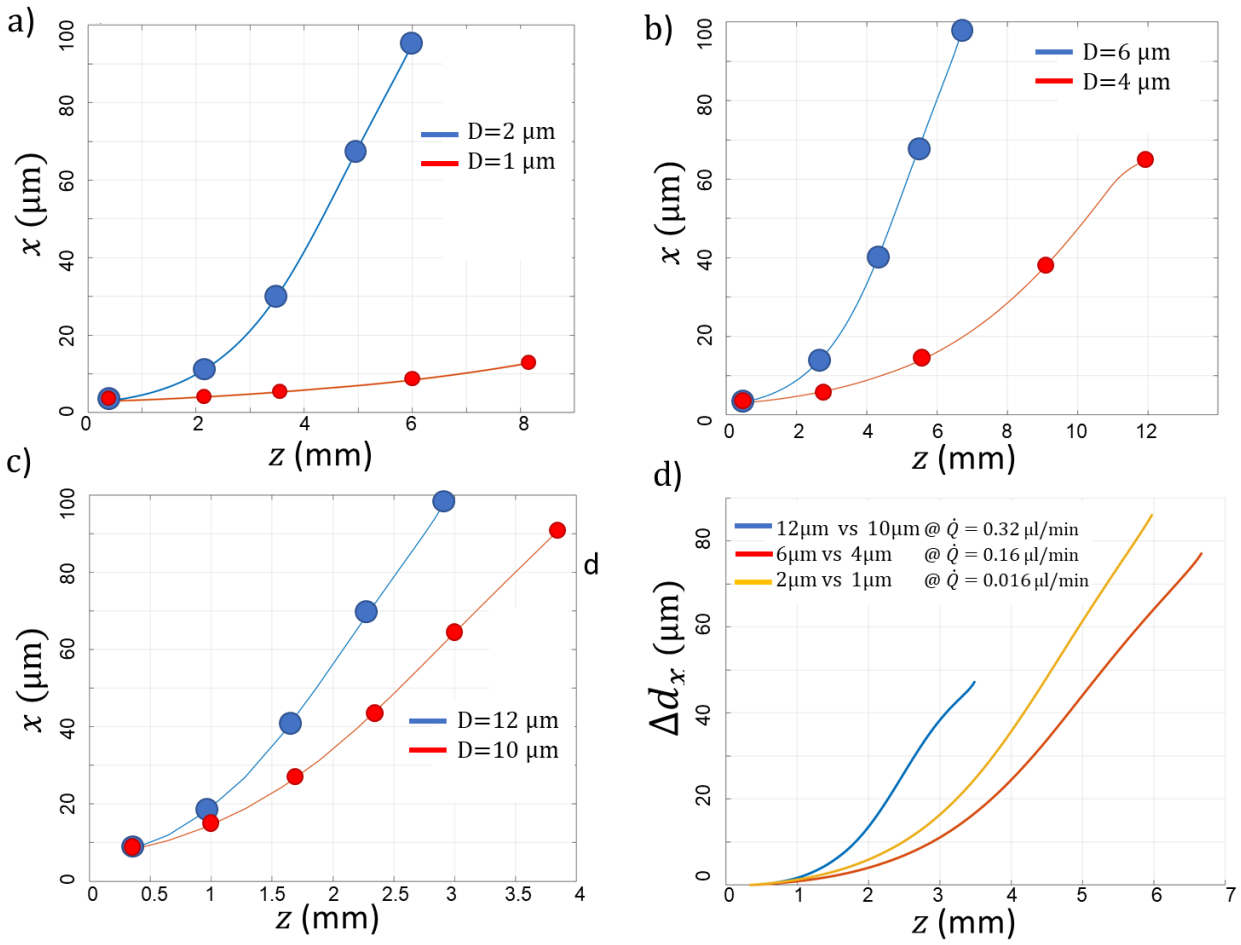

Figure 28) Separation performance of Design I (Voltage = 2V): a) Separating 2µm vs.1µm diameter particles at $\dot{Q}_{sample} = 0.016$ µl/min b) Separating 6 µm vs. 4 µm diameter particles at $\dot{Q}_{sample} = 0.16$ µl/min , c) Separating 12 µm vs. 10 µm diameter particles at $\dot{Q}_{sample} = 0.32$ µl/min , d) Comparing the maximum separation distance between each two particles

In real situations, the alignment before the separation stage is not perfect, meaning that the particles entering the separation stage have a slightly different location to the pressure node. Thus, they experience different acoustic forces from the beginning. To show the importance of perfect alignment on the efficiency of separation, another simulation is performed considering particles are aligned in a lane with the thickness of 5 µm in the x direction (for the vertical direction, random

initial locations were considered). As demonstrated in Figure 29 a-c, separation efficiency for smaller size ratios is highly dependent on the alignment efficiency. For $\{10\ \mu m$ vs. $12\ \mu m\}$ separation, the two separated streamlines highly overlap each other resulting in compromising the purity of separation, whereas for higher particle size ratios ($\{2\mu m$ vs. $1\mu m\}$), even almost perfect separation can be achieved at a proper channel length.

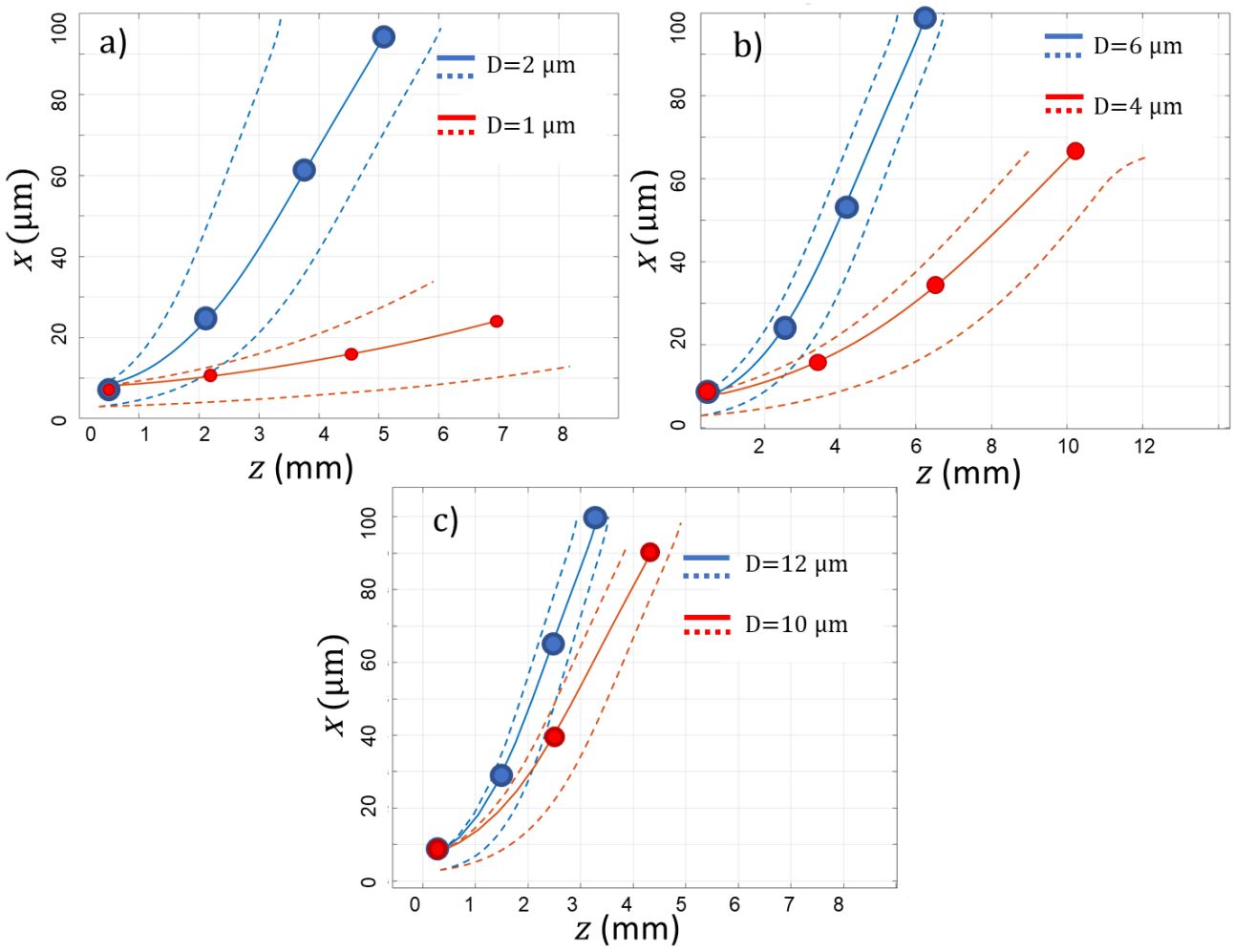

Figure 29) Separation performance of Design I assuming unperfect focusing alignment: a) Separating 2 µm vs1 µm at $\dot{Q}_{sample} = 0.016$ µl/min b) Separating 6 µm vs4 µm at $\dot{Q}_{sample} = 0.16$ µl/min , c) Separating 12 µm vs10 µm at $\dot{Q}_{sample} = 0.32$ µl/min.

Next, the separation quality in each design defined in Table 5 is compared. As shown in Figure 30, Design I result in a higher maximum separation distance, 37% more than Design III and 78% more than Design II. However, the maximum separation distance between particles happens sooner for Design II.

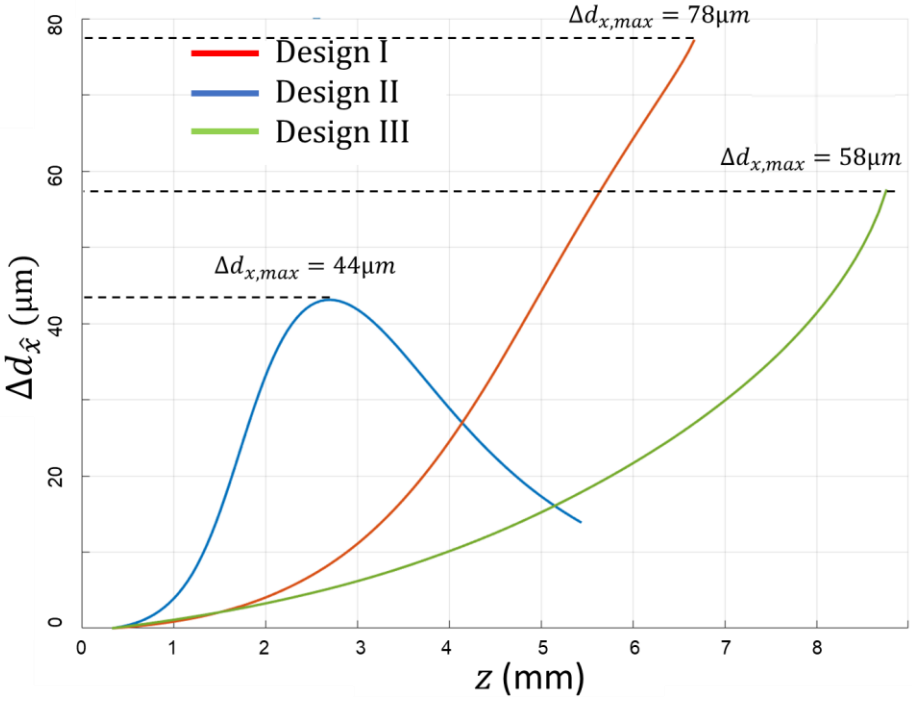

Figure 30) Comparison of the separation distance between particles (4µm vs. 6µm diameter) for each design, where $\dot{Q}_{sample} = 0.16\ \frac{\mu L}{min}$, and $Voltage = 2V$.

There are a couple of reasons for the observed discrepancies in separation performances that can be better understood by looking at each device's acoustic pressure (Figure 31) and acoustic radiation force (Figure 32) distributions.

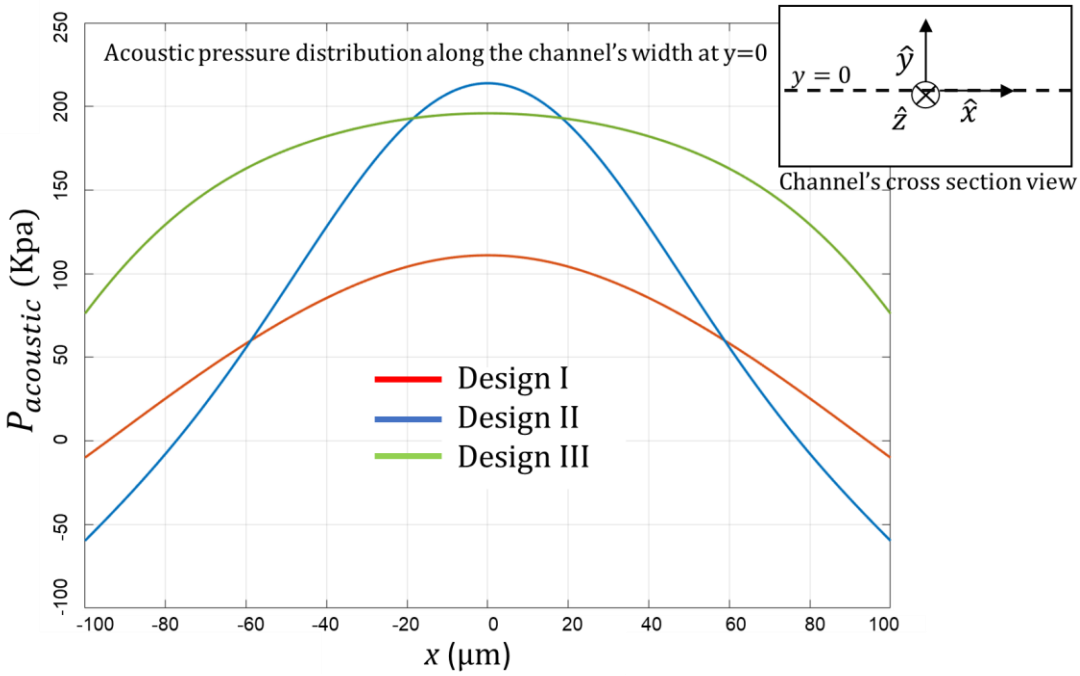

Figure 31) Acoustic pressure distribution across the channel's width at the middle of the channel's height (y=0) for each design defined in Table 5 where Voltage =2V.

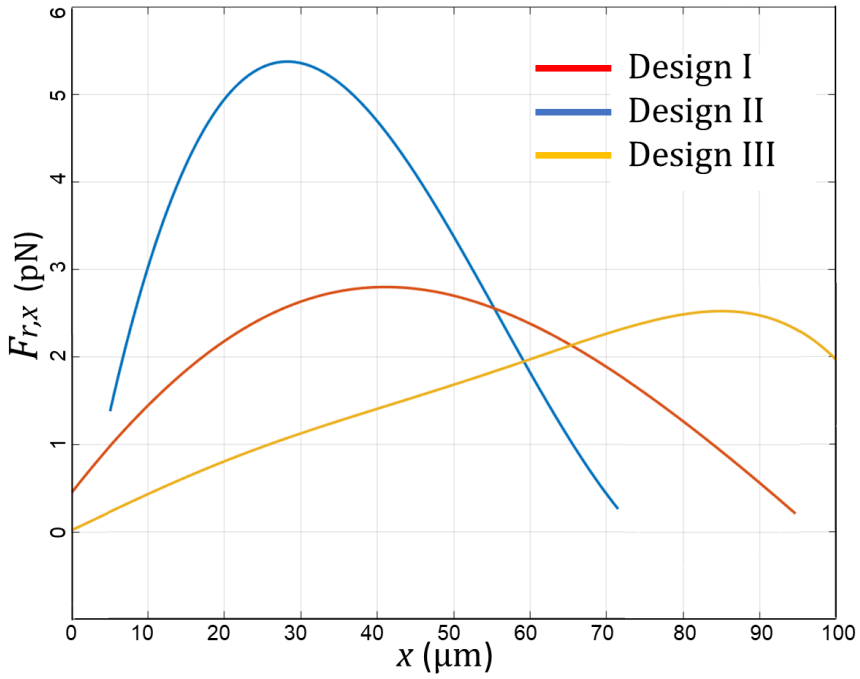

Figure 32) lateral component of acoustic radiation force across the channel's width for the three device designs

First, since the wavelength of the second design is short, two pressure nodes are located inside the channel near the walls resulting in a shorter potential distance for particles to migrate in the lateral direction for the same channel. Although, it should be mentioned that shorter wavelengths provide stronger acoustic pressure inside the channel, so less voltage will be required to achieve the maximum separation efficiency at a certain length and flow rate. Moreover, as shown in Figure 30, for Design I and Design III, the separation distance of the particles increases at a low rate near the channel's inlet and reaches its maximum value at the end, where the bigger particle approaches the channel's side wall. By looking at the acoustic radiation force applied on particles in each design (shown in Figure 32) it appears that for Design III the maximum acoustic force applied on each particle happens closer to the channel wall since the acoustic pressure has a more even distribution across the channel's width (y=0) as shown in Figure 31, causing very slow migration for particles. Moreover, Design I, which has the best separation efficiency, has a balanced acoustic pressure (and, subsequently, acoustic radiation force) distribution. In contrast, for Design II, the maximum force is experienced near the center of the channel with a sharper acoustic pressure distribution.

After conducting the previous simulations and investigating the effect of various parameters on the acoustophoretic device performance, the main findings can be listed as:

1- The thickness of PDMS walls can significantly influence the topology of pressure distribution inside the channel
2- The side sheath flow is required to confine the particles within the desired region where the direction of the acoustic radiation force is toward the channel's center.

3- For low aspect ratio channels, the PDMS wall thickness can be tuned to have wider or narrower pressure distribution across the channel width without compromising the frequency and power of the incoming waves (same wavelength but wider pressure distribution can be achieved in some cases)
4- The efficiency of the particle alignment stage has a strong influence on the efficiency of the separation stage of the device.
5- Device designs with wider pressure distribution across the channel have a more significant maximum separation distance (better efficiency) for a given flow rate and voltage at the cost of requiring a longer channel.
6- Separating large particles with similar sizes (such as 12 μm and 10 μm diameter particles) is possible when using proper channel configurations.
7- The maximum separation distance that can be achieved in each device is only a function of the ratio of the particle's diameter. At the same time, the particle flow rates and the applied voltage determine the required channel length.

4.7 Experimental results of the microparticle manipulation

In this section, a couple of experimental studies are performed to validate our numerical findings. First, we assess the particle focusing stage of the device in various operating conditions. Following that, the performance of the whole device in separating different microparticles will be demonstrated.

4.7.1 Experimental results of the particle focusing manipulation

As discussed earlier, the numerical simulation showed that the interaction of the PDMS wall would cause noticeable dislocation in PN and PAN positions inside the channel. Here, based on the design configurations investigated in the numerical section, a two-stage acoustofluidics

device was fabricated. The width and height of the microchannel and the SAW wavelength are W_C=200 μm , H_C=100μm, and λ_{SAW}=400μm, respectively. PS particle with the size of 5 μm was injected into the channel at the rate of 2 $\mu L/min$, and the voltage was set to be 10 V. As it is shown in Figure 33, particles are aligned in three lanes, including the center pressure node line as well as two lanes at the walls of the channel which indicates that there are two pressure anti-nodes (PAN) located inside the channel somewhere in between the center and PDMS walls which is in complete agreement with the numerical result where we also observed two pressure anti-nodes inside the microchannel (see Figure 17).

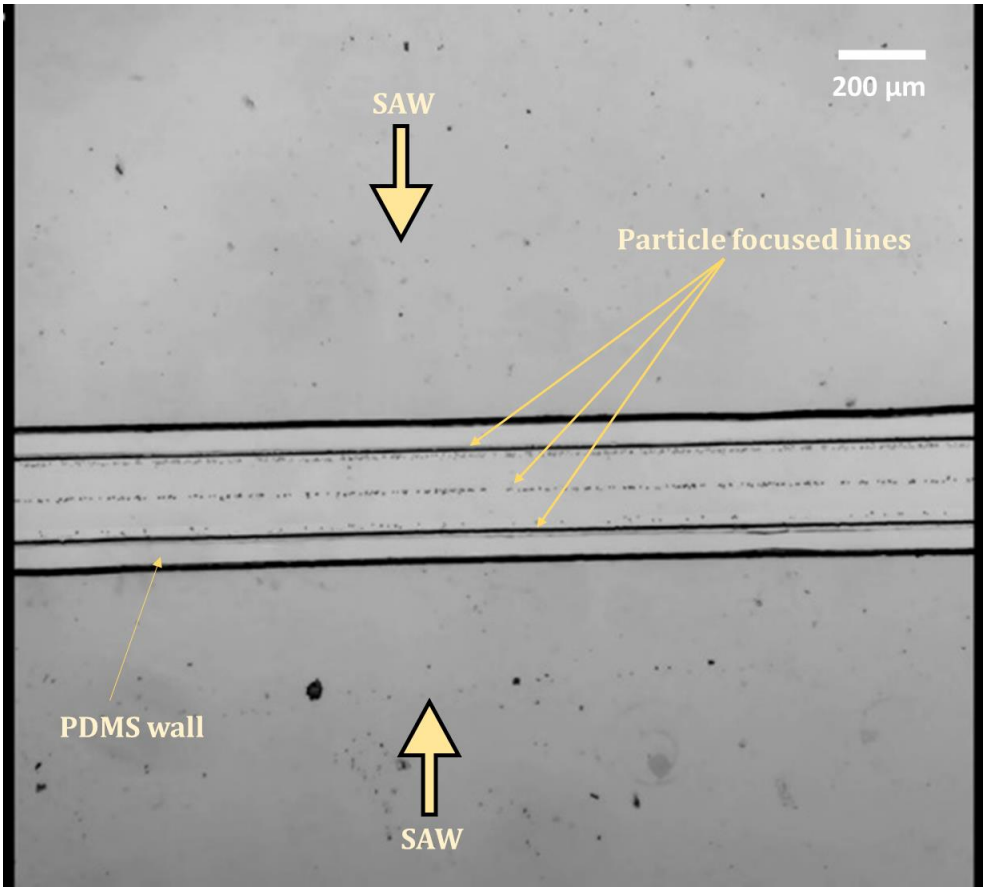

Figure 33) Microscopic view of focused $5\mu m$ diameter microparticles $\dot{Q}_{Sheath} = 0,\ \dot{Q}_{sample} = 2\mu L/min$

To be able to find the exact location of the pressure anti-nodes, the sheath flow rate was gradually increased from 0 with the increment of $\dot{Q}_{sample}/8$ until at $\dot{Q}_{Sheath} \approx 6/8\dot{Q}_{sample}$ (75% of the sample flow rate) the two particle focusing lines near the walls started to disappear and only one focusing line at the center remained. Based on that, as shown in Figure 34 the location of PANs are estimated to be ~43µm away from the side walls. This is in good agreement with our numerical simulation represented in Figure 17 where the PANs are located inside the channel ~50 µm away from the side walls.

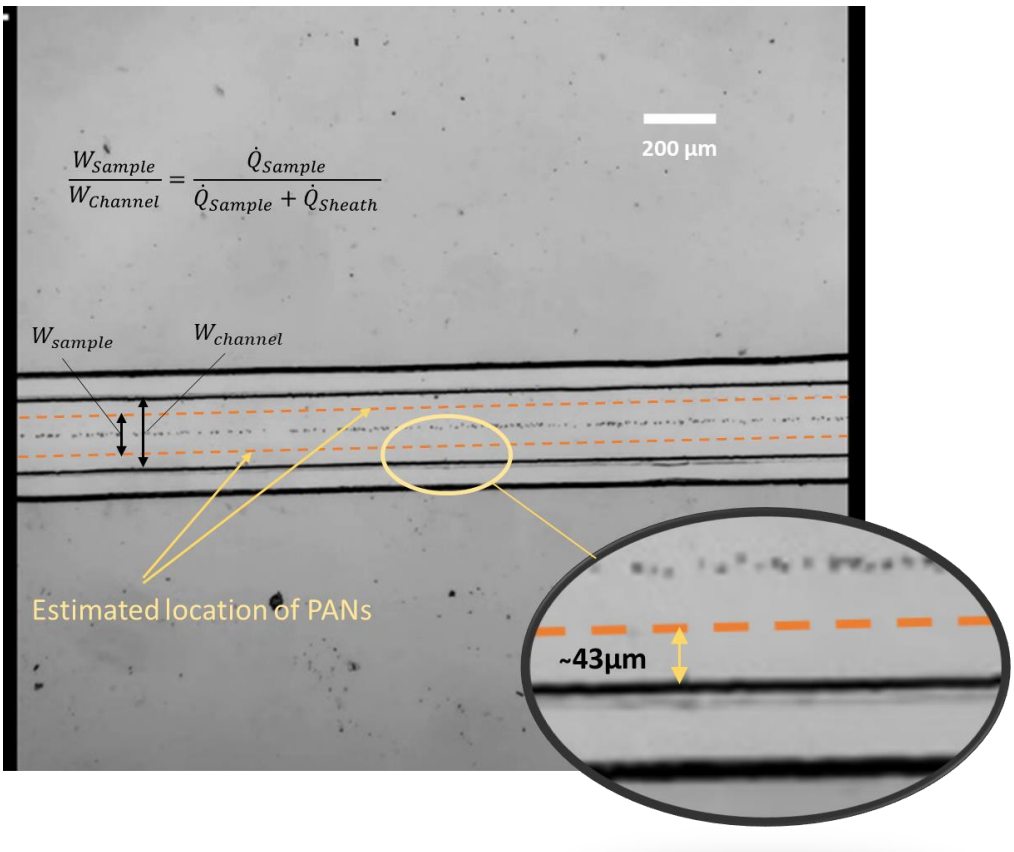

Figure 34) Location of the pressure anti-nodes inside the microchannel at the focusing stage

4.7.2 Experimental results of the particle separation stage

After evaluating the focusing module of the device, in this part, the separation of microparticles is experimentally evaluated. Two critical parameters for any particle separation devices are throughput and purity rate. For the following experiments, these two parameters will be observed to assess the functionality of the designed SSAW devise.

Here to measure the purity rates, after collecting the microparticles from each outlet, the particles are dispersed on the surface of a hydrophobic glass. The glass is then placed on a hot plate to evaporate the remaining water. Eventually, the distribution of particles will be captured under the microscope in 10 random locations on the glass substrate (Figure 35). Particle counting was performed for each captured image using the image processing technique (ImageJ Software). By defining the purity rate as the number of counted target particles per total number of particles collected from each outlet, the average purity rate of each outlet was calculated.

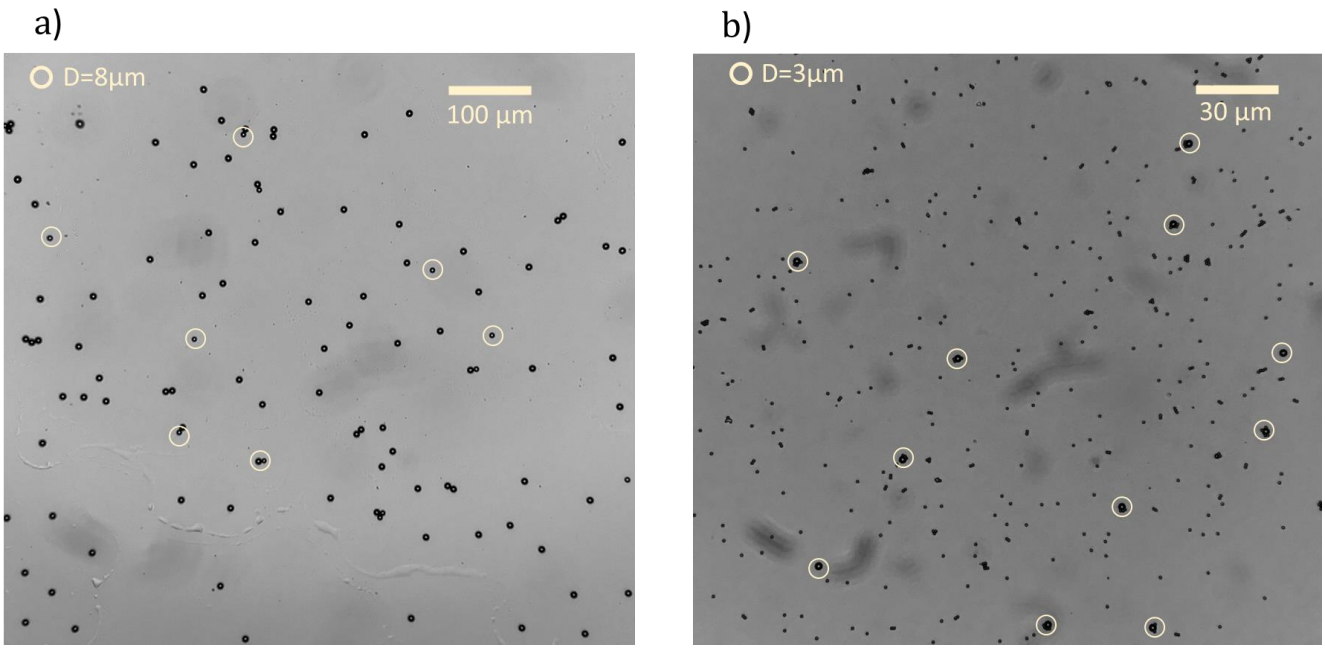

Figure 35) An image of collected particles from outlets in different tests a) 10µ$\boldsymbol{m}$ and 8µ$\boldsymbol{m}$ diameter particles collected from outlet 1 b) 3µ$\boldsymbol{m}$ and 1µ$\boldsymbol{m}$ diameter particles collected from outlet 2

In order to evaluate the performance of the device in separating microparticles, two binary separations (3 µm from 1 µm) and (10 µm from 8 µm) at different flow rates and applied voltages were performed, and the results are shown in Table **6**.

Table 6) The results of binary separation of (3 µm from 1 µm diameter) and (10 µm from 8 µm diameter) microparticles under different voltage and flowrates

Diameters of the particles	**Sample flow rate ($\dot{Q}_{sample}$) (µL/min)**	**Voltage (V)**	**Purity rate outlet 1 (bigger particle)**	**Purity rate outlet 2 (smaller particle)**
3 µm vs 1 µm	2	10	94%	92%
3 µm vs 1 µm	8	25	92%	85%
3 µm vs 1 µm	12	25	98%	53%
10 µm vs 8 µm	10	10	91%	80%
10 µm vs 8 µm	15	25	83%	70%
10 µm vs 8 µm	19	25	93%	61%

As expected, the separation of 1 µm from 3 µm was performed with a high purity rate (>92% for the 3µm diameter particle and >85% for the 1 µm) for the first two experiments. However, the result of the second experiment shows that increasing the flow rate to 12 µL/min has drastically decreased the purity rate of the 1 µm diameter particle while the 3 µm diameter particle purity rate is 98%. This indicates that in applications where the purification of the larger particle is of most importance, higher throughput can be achieved at the cost of reducing the recovery rate (number of particles entered per number of particles extracted from the desired outlet). Furthermore, the main reason that even with lower flow rates, the purity rate of separating 3 µm diameter particles is not 100% is that particles also receive the acoustic force in the vertical

direction, causing them to adhere to the PDMS walls on top of the channel and experiencing different path toward the end of the channel. Moreover, due to the possible insufficient acoustic radiation force at the focusing stage, some smaller particles might not reach the desired focusing thickness, hence exiting the wrong outlet.

For the case of separating 10µm from 8µm particles, the purity rates of 10µm particles at different experiments are 91%, 83%, and 87% (outlet1), whereas the purity rates for the 8µm particles are lower than those for 10µm (93%, 70%, and 61% for the first, second and third experiment respectively).

Moreover, For the case of separating 10µm from 8µm diameter particles, higher throughput was achieved since the sizes of the particles are larger compared to the first set of particles (3µm vs. 1µm). Although, the purity rate of separation was lower than the first set of particles as expected. It should also be mentioned that the flow characteristic can be set to have more purity rate for one of the particles (larger one) at the cost of losing the recovery rate and also reducing the purity rate of the other particle. Figure 36 shows examples of microparticle separation with different sizes. Overall, the experimental results indicate that using two-stage acoustofluidic device with a proper design for the channel dimension and the acquired wavelength is strongly capable of separating particles with similar sizes at high throughput and acceptable purity rate.

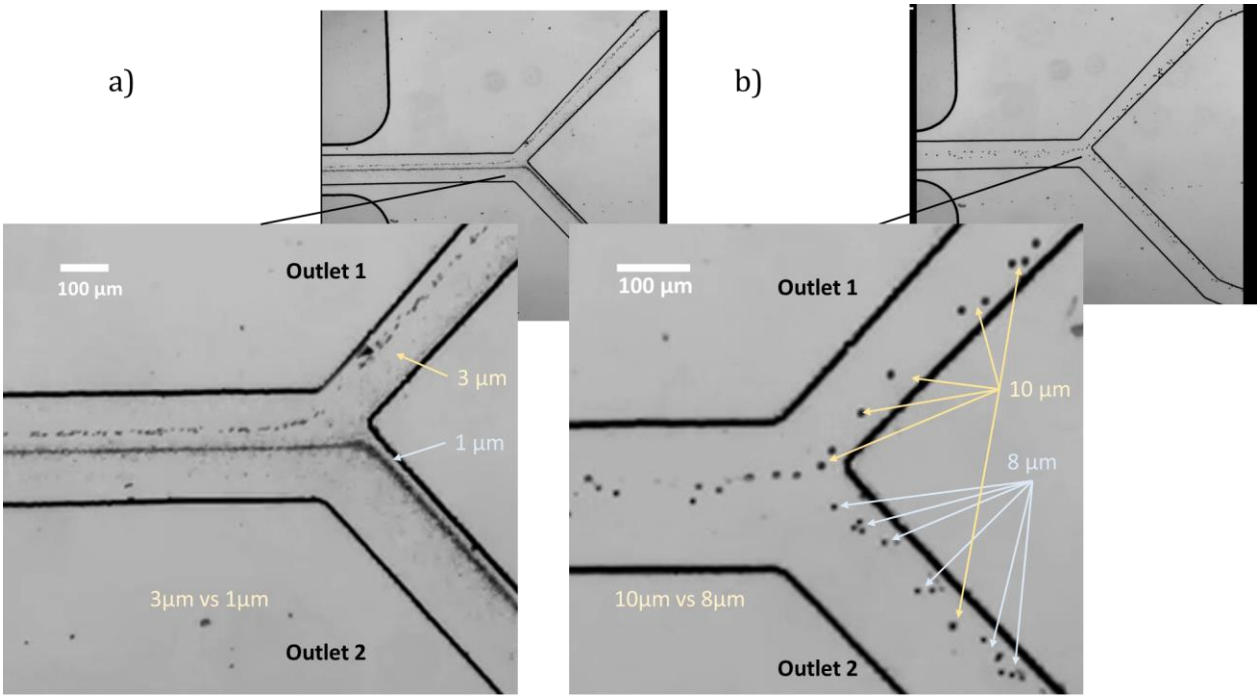

Figure 36) Microscopic images of separating different particles: a) 1 µm vs. 3 µm diameters where $\dot{Q}_{sample}$ = 8 µL/min, and Voltage = 25 V b) 10 µm vs. 8 µm diameters, where $\dot{Q}_{sample}$ = 3 µL/min, and Voltage = 10 V

Chapter 5: Final remarks

5.1 Conclusion

One of the objectives of this study was to show that the acoustofluidic chip provides a highly precise and rapid-acting platform for microparticle manipulation and separation. To accomplish this objective, numerous procedures were performed, including parameter optimization, development of 2D and 3D numerical simulations, and experimentation. Initially, the suggested two-stage paSSAW acoustofluidics chip was analyzed parametrically using FEM. This step was required to comprehend the processes occurring on the chip. The optimal parameter values were determined using numerical simulation. The numerical study of IDT configurations revealed that the number of fingers plays a pivotal role in the efficiency of the power transmission through the IDTs. Moreover, through experimental measurement an efficient IDT design was chosen for the acoustofluidics platform.

Next, investigating the effect of PDMS wall thickness on the acoustic pressure distribution inside the channel and the subsequent particle tracking studies for the focusing/separation modules demonstrated that:

- The thickness of PDMS walls can significantly influence the topology of pressure distribution inside the channel
- For low aspect ratio channels, the PDMS wall thickness can be tuned to have broader or narrower pressure distribution across the channel width without compromising the frequency and power of the incoming waves (same wavelength but wider pressure distribution can be achieved in some cases).
- An optimized side sheath flow rate can be chosen to effectively assist the acoustic radiation force in focusing particles.

- The efficiency of the particle alignment stage has a strong influence on the efficiency of the separation stage of the device.
- Acoustic designs with broader pressure distribution across the channel have larger maximum separation distance (better efficiency) for a given flow rate and voltage at the cost of requiring a longer channel.
- Separating large particles with similar sizes is possible using proper IDT/channel configurations.
- The maximum separation distance that can be achieved in each design is significantly dependent on the ratio of the particle's diameter, while the particle flow rate, and the applied voltage determine the required channel length to meet the maximum separation distance.

Finally, the numerically optimized design was experimentally evaluated. After validating the numerical results, it was shown that the fabricated chip could separate 10μm from 8μm diameter particles with a high throughput of 10 μL/min and an acceptable purity rate of >80%.

5.2 Future work

The capability of the suggested acoustofluidic chip to manipulate and separate synthetic (PS) microparticles has been demonstrated. Some of the bioparticle's physical properties (such as compressibility) differ slightly from those of PS particles, necessitating the repetition of a study using bioparticles in future research.

The capability of the proposed design in separating more than two particles at the same time should be investigated.

Integrating the features of acoustofluidics with other active/passive separation methods should be thoroughly investigated.

One subject that needs to be studied more is the application of machine learning in optimizing different features of particle manipulation.

Finally, the potential of commercialization of such techniques by reducing the power consumption, simplifying and automation is an interesting area to consider for future researches.

Bibliography

[1] E. van Voorthuizen, A. Zwijnenburg, W. van der Meer, and H. Temmink, "Biological black water treatment combined with membrane separation," *Water Res*, vol. 42, no. 16, pp. 4334–4340, 2008, doi: 10.1016/J.WATRES.2008.06.012.

[2] J. Zhou, A. Kulasinghe, A. Bogseth, K. O'Byrne, C. Punyadeera, and I. Papautsky, "Isolation of circulating tumor cells in non-small-cell-lung-cancer patients using a multi-flow microfluidic channel," *Microsystems & Nanoengineering 2019 5:1*, vol. 5, no. 1, pp. 1–12, Feb. 2019, doi: 10.1038/s41378-019-0045-6.

[3] S. Yan and D. Yuan, "Continuous microfluidic 3D focusing enabling microflow cytometry for single-cell analysis," *Talanta*, vol. 221, p. 121401, Jan. 2021, doi: 10.1016/J.TALANTA.2020.121401.

[4] M. Wu, A. Ozcelik, J. Rufo, Z. Wang, R. Fang, and T. Jun Huang, "Acoustofluidic separation of cells and particles," *Microsystems & Nanoengineering 2019 5:1*, vol. 5, no. 1, pp. 1–18, Jun. 2019, doi: 10.1038/s41378-019-0064-3.

[5] R. Nasiri *et al.*, "Microfluidic-Based Approaches in Targeted Cell/Particle Separation Based on Physical Properties: Fundamentals and Applications," *Small*, vol. 16, no. 29, p. 2000171, Jul. 2020, doi: 10.1002/SMLL.202000171.

[6] F. Li, F. Li, D. Luo, W. Lai, Y. Xiong, and H. Xu, "Biotin-exposure-based immunomagnetic separation coupled with nucleic acid lateral flow biosensor for visibly detecting viable Listeria monocytogenes," *Anal Chim Acta*, vol. 1017, pp. 48–56, Aug. 2018, doi: 10.1016/J.ACA.2018.02.009.

[7] I. Antoniadi *et al.*, “Fluorescence activated cell sorting—A selective tool for plant cell isolation and analysis,” *Cytometry Part A*, vol. 101, no. 9, pp. 725–736, Sep. 2022, doi: 10.1002/CYTO.A.24461.

[8] A. Bøyum, “[9] Separation of lymphocytes, granulocytes, and monocytes from human blood using iodinated density gradient media,” *Methods Enzymol*, vol. 108, no. C, pp. 88–102, Jan. 1984, doi: 10.1016/S0076-6879(84)08076-9.

[9] W. Lee, P. Tseng, and D. di Carlo, “Microfluidic Cell Sorting and Separation Technology,” pp. 1–14, 2017, doi: 10.1007/978-3-319-44139-9_1.

[10] N. Azizipour, R. Avazpour, D. Rosenzweig, M. S.- Micromachines, and undefined 2020, “Evolution of biochip technology: A review from lab-on-a-chip to organ-on-a-chip,” *mdpi.com*, doi: 10.3390/mi11060599.

[11] N. Nguyen, S. Wereley, and S. Shaegh, *Fundamentals and applications of microfluidics*. 2019. Accessed: Oct. 28, 2022. [Online]. Available: https://books.google.ca/books?hl=en&lr=&id=h3iFDwAAQBAJ&oi=fnd&pg=PP1&dq=benefits+of+microfluidics&ots=e92ANtqY-U&sig=HYqLnUr5AgVBMuT4-ZWoHEDWDgg

[12] J. Lafleur, A. Jönsson, S. Senkbeil, J. K. Bioelectronics, and undefined 2016, “Recent advances in lab-on-a-chip for biosensing applications,” *Elsevier*, Accessed: Oct. 28, 2022. [Online]. Available: https://www.sciencedirect.com/science/article/pii/S0956566315303298

[13] N. Lion *et al.*, “Proteomics in Microfluidic Devices,” *microfluidics.utoronto.ca*, vol. 24, no. 21, pp. 3533–3562, Nov. 2003, doi: 10.1002/elps.200305629.

[14] E. Esch, A. Bahinski, D. H.-N. reviews D. discovery, and undefined 2015, "Organs-on-chips at the frontiers of drug discovery," *nature.com*, Accessed: Oct. 28, 2022. [Online]. Available: https://www.nature.com/articles/nrd4539

[15] G. Du, Q. Fang, and J. M. J. den Toonder, "Microfluidics for cell-based high throughput screening platforms—A review," *Anal Chim Acta*, vol. 903, pp. 36–50, Jan. 2016, doi: 10.1016/J.ACA.2015.11.023.

[16] X. Chen, D. F. Cui, C. C. Liu, and H. Li, "Microfluidic chip for blood cell separation and collection based on crossflow filtration," *Sens Actuators B Chem*, vol. 130, no. 1, pp. 216–221, Mar. 2008, doi: 10.1016/J.SNB.2007.07.126.

[17] N. Xiang, J. Wang, Q. Li, Y. Han, D. Huang, and Z. Ni, "Precise Size-Based Cell Separation via the Coupling of Inertial Microfluidics and Deterministic Lateral Displacement," *Anal Chem*, vol. 91, no. 15, pp. 10328–10334, Aug. 2019, doi: 10.1021/ACS.ANALCHEM.9B02863.

[18] H. Shirinkami, G. Wang, J. Park, J. Ahn, … Y. C.-S. and A. B., and undefined 2020, "Red blood cell and white blood cell separation using a lateral-dimension scalable microchip based on hydraulic jump and sedimentation," *Elsevier*, Accessed: Oct. 28, 2022. [Online]. Available: https://www.sciencedirect.com/science/article/pii/S0925400519316119?casa_token=QSIVvCmdyS4AAAAA:J0aXprAWW5mKfuozhr118yUKQE87K0UZJW3iogl4CdO9tj3gc0u9VA33-TbS0Ns4qlQd9wx7

[19] G. Y. Kim, J. I. Han, and J. K. Park, "Inertial Microfluidics-Based Cell Sorting," *Biochip J*, vol. 12, no. 4, pp. 257–267, Dec. 2018, doi: 10.1007/S13206-018-2401-2.

[20] Y. Huang *et al.*, “Electric manipulation of bioparticles and macromolecules on microfabricated electrodes,” *Anal Chem*, vol. 73, no. 7, pp. 1549–1559, Apr. 2001, doi: 10.1021/AC001109S.

[21] A. Surendran, R. Zhou, Y. L.-J. of Medical, and undefined 2021, “Microfluidic devices for magnetic separation of biological particles: A review,” *asmedigitalcollection.asme.org*, Accessed: Oct. 28, 2022. [Online]. Available: https://asmedigitalcollection.asme.org/medicaldevices/article-abstract/15/2/024001/1089138

[22] M. G.-A. A. united with Acustica and undefined 1998, “Ultrasonic separation of suspended particles-Part I: Fundamentals,” *ingentaconnect.com*, Accessed: Oct. 28, 2022. [Online]. Available: https://www.ingentaconnect.com/content/dav/aaua/1998/00000084/00000003/art00006

[23] A. Jonáš and P. Zemánek, “Light at work: The use of optical forces for particle manipulation, sorting, and analysis,” *Electrophoresis*, vol. 29, no. 24, pp. 4813–4851, Dec. 2008, doi: 10.1002/ELPS.200800484.

[24] F. Shiri, H. Feng, B. G.-P. S. Techniques, and undefined 2022, “Passive and active microfluidic separation methods,” *Elsevier*, Accessed: Oct. 28, 2022. [Online]. Available: https://www.sciencedirect.com/science/article/pii/B9780323854863000135

[25] M. Sivaramakrishnan, … R. K.-C. O. in, and undefined 2020, “Active microfluidic systems for cell sorting and separation,” *Elsevier*, Accessed: Oct. 28, 2022. [Online]. Available: https://www.sciencedirect.com/science/article/pii/S2468451119300492?casa_token=NTs

Mw9mIkCIAAAAA:k7_k5q3aAGnQg2mxc5EAXvs7qP4NWofBPpO24-kZoK72xhhQgFDYbB0FHfuX1ewngU4drptq

[26] A. Nakano, A. R.- Electrophoresis, and undefined 2013, "Protein dielectrophoresis: advances, challenges, and applications," *Wiley Online Library*, vol. 34, no. 7, pp. 1085–1096, Apr. 2013, doi: 10.1002/elps.201200482.

[27] J. Lim, S. P. Yeap, and S. C. Low, "Challenges associated to magnetic separation of nanomaterials at low field gradient," *Sep Purif Technol*, vol. 123, pp. 171–174, Feb. 2014, doi: 10.1016/J.SEPPUR.2013.12.038.

[28] W. Connacher, N. Zhang, A. Huang, J. Mei, S. Z.-L. on a Chip, and undefined 2018, "Micro/nano acoustofluidics: materials, phenomena, design, devices, and applications," *pubs.rsc.org*, Accessed: Oct. 28, 2022. [Online]. Available: https://pubs.rsc.org/en/content/articlehtml/2017/sc/c8lc00112j

[29] R. Nasiri *et al.*, "Microfluidic-based approaches in targeted cell/particle separation based on physical properties: Fundamentals and applications," *Wiley Online Library*, vol. 16, no. 29, Jul. 2020, doi: 10.1002/smll.202000171.

[30] W. Connacher *et al.*, "Micro/nano acoustofluidics: materials, phenomena, design, devices, and applications," *Lab Chip*, vol. 18, no. 14, pp. 1952–1996, Jul. 2018, doi: 10.1039/C8LC00112J.

[31] K. Länge, "Bulk and Surface Acoustic Wave Sensor Arrays for Multi-Analyte Detection: A Review," *Sensors 2019, Vol. 19, Page 5382*, vol. 19, no. 24, p. 5382, Dec. 2019, doi: 10.3390/S19245382.

[32] D. Mandal and S. Banerjee, “Surface Acoustic Wave (SAW) Sensors: Physics, Materials, and Applications,” *Sensors 2022, Vol. 22, Page 820*, vol. 22, no. 3, p. 820, Jan. 2022, doi: 10.3390/S22030820.

[33] Y. Liu, Y. Cai, Y. Zhang, A. Tovstopyat, S. Liu, and C. Sun, “Materials, Design, and Characteristics of Bulk Acoustic Wave Resonator: A Review,” *Micromachines 2020, Vol. 11, Page 630*, vol. 11, no. 7, p. 630, Jun. 2020, doi: 10.3390/MI11070630.

[34] G. P. Gautam, T. Burger, A. Wilcox, M. J. Cumbo, S. W. Graves, and M. E. Piyasena, “Simple and inexpensive micromachined aluminum microfluidic devices for acoustic focusing of particles and cells,” *Anal Bioanal Chem*, vol. 410, no. 14, pp. 3385–3394, May 2018, doi: 10.1007/S00216-018-1034-6/FIGURES/6.

[35] W. Connacher, N. Zhang, A. Huang, J. Mei, S. Z.-L. on a Chip, and undefined 2018, “Micro/nano acoustofluidics: materials, phenomena, design, devices, and applications,” *pubs.rsc.org*, Accessed: Oct. 28, 2022. [Online]. Available: https://pubs.rsc.org/en/content/articlehtml/2017/sc/c8lc00112j

[36] D. Mandal, S. B.- Sensors, and undefined 2022, “Surface acoustic wave (SAW) sensors: Physics, materials, and applications,” *mdpi.com*, vol. 22, p. 820, 2022, doi: 10.3390/s22030820.

[37] N. Afsarimanesh, A. Nag, M. E. E. Alahi, T. Han, and S. C. Mukhopadhyay, “Interdigital sensors: Biomedical, environmental and industrial applications,” *Sens Actuators A Phys*, vol. 305, p. 111923, Apr. 2020, doi: 10.1016/J.SNA.2020.111923.

[38] X. Lu, M. Tayebi, Y. A.- Electrophoresis, and undefined 2021, “A low-cost and high-throughput benchtop cell sorter for isolating white blood cells from whole blood,” *Wiley*

Online Library, vol. 42, no. 21–22, pp. 2281–2292, Nov. 2021, doi: 10.1002/elps.202100024.

[39] S. Ning *et al.*, "A microfluidic chip with a serpentine channel enabling high-throughput cell separation using surface acoustic waves," *pubs.rsc.org*, Accessed: Oct. 28, 2022. [Online]. Available: https://pubs.rsc.org/en/content/articlehtml/2021/xx/d1lc00840d

[40] A. Urbansky, P. Ohlsson, A. Lenshof, F. G.-S. reports, and undefined 2017, "Rapid and effective enrichment of mononuclear cells from blood using acoustophoresis," *nature.com*, Accessed: Oct. 28, 2022. [Online]. Available: https://www.nature.com/articles/s41598-017-17200-9

[41] S. Liu, P. Yoo, N. Garg, A. Lee, S. R.-S. and A. A, and undefined 2021, "A microfluidic device for blood plasma separation and fluorescence detection of biomarkers using acoustic microstreaming," *Elsevier*, Accessed: Oct. 28, 2022. [Online]. Available: https://www.sciencedirect.com/science/article/pii/S0924424720317970

[42] C. Magnusson, P. Augustsson, A. Lenshof, Y. Ceder, T. Laurell, and H. Lilja, "Clinical-Scale Cell-Surface-Marker Independent Acoustic Microfluidic Enrichment of Tumor Cells from Blood," *Anal Chem*, vol. 89, no. 22, pp. 11954–11961, Nov. 2017, doi: 10.1021/ACS.ANALCHEM.7B01458.

[43] X. Bai *et al.*, "Postoperative evaluation of tumours based on label-free acoustic separation of circulating tumour cells by microstreaming," *pubs.rsc.org*, Accessed: Oct. 28, 2022. [Online]. Available: https://pubs.rsc.org/en/content/articlehtml/2021/lc/d1lc00165e?casa_token=SfjQZpnDzEEAAAAA:j276N0bCXMawuytlNT5FEJg8gpI6BVSYMaKNVSHHibFR4rH9wXB9v6UpGXOs1Nn5reuceaTzCYlO

[44] J. Detzner, D. Steil, G. Pohlentz, N. Legros, and J. Müthing, “Surface acoustic wave (SAW) real-time interaction analysis of influenza A virus hemagglutinins with sialylated neoglycolipids,” *Glycobiology*, vol. 31, no. 7, pp. 734–740, Aug. 2021, doi: 10.1093/GLYCOB/CWAB009.

[45] Y. Ai, C. Sanders, B. M.-A. chemistry, and undefined 2013, “Separation of Escherichia coli Bacteria from Peripheral Blood Mononuclear Cells Using Standing Surface Acoustic Waves,” *ACS Publications*, vol. 85, no. 19, pp. 9126–9134, Oct. 2013, doi: 10.1021/ac4017715.

[46] K. P. Kulkarni, S. H. Ramarathinam, J. Friend, L. Yeo, A. W. Purcell, and P. Perlmutter, “Rapid microscale in-gel processing and digestion of proteins using surface acoustic waves,” *Lab Chip*, vol. 10, no. 12, pp. 1518–1520, Jun. 2010, doi: 10.1039/C001501F.

[47] M. Wu *et al.*, “Isolation of exosomes from whole blood by integrating acoustics and microfluidics,” *Proc Natl Acad Sci U S A*, vol. 114, no. 40, pp. 10584–10589, Oct. 2017, doi: 10.1073/PNAS.1709210114.

[48] Z. Wang *et al.*, “Acoustofluidic salivary exosome isolation: a liquid biopsy compatible approach for human papillomavirus–associated oropharyngeal cancer detection,” *Elsevier*, Accessed: Oct. 28, 2022. [Online]. Available: https://www.sciencedirect.com/science/article/pii/S1525157819303952

[49] S. Ning *et al.*, “A microfluidic chip with a serpentine channel enabling high-throughput cell separation using surface acoustic waves,” *pubs.rsc.org*, Accessed: Oct. 30, 2022. [Online]. Available: https://pubs.rsc.org/en/content/articlehtml/2021/xx/d1lc00840d?casa_token=VdoSm0IWK

gYAAAAA:O0xNZjVnQ0nRwVNWl9w6J5zE3xYICJxWak3sy1PEKyuYyI-C36xvzmi5IGSowIoa_XS9YflvK2rW

[50] S. Li, F. Ma, H. Bachman, C. E. Cameron, X. Zeng, and T. J. Huang, "Acoustofluidic bacteria separation," *Journal of Micromechanics and Microengineering*, vol. 27, no. 1, p. 015031, Nov. 2016, doi: 10.1088/1361-6439/27/1/015031.

[51] J. Nam, H. Lim, D. Kim, S. S.-L. on a Chip, and undefined 2011, "Separation of platelets from whole blood using standing surface acoustic waves in a microchannel," *pubs.rsc.org*, Accessed: Oct. 30, 2022. [Online]. Available: https://pubs.rsc.org/en/content/articlehtml/2011/lc/c1lc20346k?casa_token=Y57DpPFilsEAAAAA:BPRR8I6erh-tZRjfz__0YdKX5xl68XTzLhGX59e0LqPjskbdRQ78ib03w8d4Yd92OK8cz54DAWr6

[52] Y. Chen *et al.*, "High-throughput acoustic separation of platelets from whole blood," *ncbi.nlm.nih.gov*, Accessed: Oct. 30, 2022. [Online]. Available: https://www.ncbi.nlm.nih.gov/pmc/articles/PMC5010861/

[53] M. Wu, A. Ozcelik, J. Rufo, Z. Wang, … R. F.-M. &, and undefined 2019, "Acoustofluidic separation of cells and particles," *nature.com*, Accessed: Oct. 29, 2022. [Online]. Available: https://www.nature.com/articles/s41378-019-0064-3

[54] X. Lu, M. Tayebi, and Y. Ai, "A low-cost and high-throughput benchtop cell sorter for isolating white blood cells from whole blood," *Electrophoresis*, vol. 42, no. 21–22, pp. 2281–2292, Nov. 2021, doi: 10.1002/ELPS.202100024.

[55] T. Peng, M. Zhou, S. Yuan, C. Fan, B. J.-A. M. Modelling, and undefined 2022, "Numerical investigation of particle deflection in tilted-angle standing surface acoustic

wave microfluidic devices," *Elsevier*, Accessed: Oct. 28, 2022. [Online]. Available: https://www.sciencedirect.com/science/article/pii/S0307904X21003437

[56] Y. Zhang, X. C.-U. Sonochemistry, and undefined 2021, "Particle separation in microfluidics using different modal ultrasonic standing waves," *Elsevier*, Accessed: Oct. 28, 2022. [Online]. Available: https://www.sciencedirect.com/science/article/pii/S1350417721001450

[57] M. Wu *et al.*, "Circulating Tumor Cell Phenotyping via High-Throughput Acoustic Separation," *Wiley Online Library*, vol. 14, no. 32, Aug. 2018, doi: 10.1002/smll.201801131.

[58] D. Collins, R. O'Rorke, A. Neild, J. Han, Y. A.-S. Matter, and undefined 2019, "Acoustic fields and microfluidic patterning around embedded micro-structures subject to surface acoustic waves," *pubs.rsc.org*, Accessed: Oct. 28, 2022. [Online]. Available: https://pubs.rsc.org/en/content/articlehtml/2019/sm/c9sm00946a?casa_token=NYMcLTUCX7IAAAAA:oVzUOOrzrNwmMDOhQWGBY50z5vAZ5q1WD_t4gAUWI25JtG1GznqWniNcr1nP1chc2uW_ZrgyDAg4

[59] N. Nama, R. Barnkob, Z. Mao, C. Kähler, F. C.-L. on a Chip, and undefined 2015, "Numerical study of acoustophoretic motion of particles in a PDMS microchannel driven by surface acoustic waves," *pubs.rsc.org*, Accessed: Oct. 28, 2022. [Online]. Available: https://pubs.rsc.org/en/content/articlehtml/2015/lc/c5lc00231a

[60] J. Hsu, C. Hsu, Y. H.- Micromachines, and undefined 2019, "Acoustophoretic control of microparticle transport using dual-wavelength surface acoustic wave devices," *mdpi.com*, doi: 10.3390/mi10010052.

[61] D. Collins, R. O'Rorke, A. Neild, J. Han, Y. A.-S. Matter, and undefined 2019, "Acoustic fields and microfluidic patterning around embedded micro-structures subject to surface acoustic waves," *pubs.rsc.org*, Accessed: Oct. 28, 2022. [Online]. Available: https://pubs.rsc.org/en/content/articlehtml/2019/sm/c9sm00946a

[62] J. Gualtieri, … J. K.-I. T. on, and undefined 1994, "Piezoelectric materials for acoustic wave applications," *ieeexplore.ieee.org*, Accessed: Oct. 30, 2022. [Online]. Available: https://ieeexplore.ieee.org/abstract/document/265820/?casa_token=afXKkcI3f84AAAAA:5bOw1MydXmPHpDLdlH0E7vywuamfkW6GWGKTno0LLkIUXxeZ9bP6pcI73t3NriW8GGlbodkL

[63] S. R. Winzer, N. Shankar, and A. P. Ritter, "Designing Cofired Multilayer Electrostrictive Actuators for Reliability," *Journal of the American Ceramic Society*, vol. 72, no. 12, pp. 2246–2257, 1989, doi: 10.1111/J.1151-2916.1989.TB06069.X.

[64] L. Thevenard *et al.*, "Irreversible magnetization switching using surface acoustic waves," *Phys Rev B Condens Matter Mater Phys*, vol. 87, no. 14, Apr. 2013, doi: 10.1103/PHYSREVB.87.144402.

[65] L. V.-M. I. R. Sviaz and undefined 1988, "Electromagnetic waves," *ui.adsabs.harvard.edu*, Accessed: Oct. 30, 2022. [Online]. Available: https://ui.adsabs.harvard.edu/abs/1988MIzRS....Q....V/abstract

[66] J. Dual, D. M.-L. on a Chip, and undefined 2012, "Acoustofluidics 4: Piezoelectricity and application in the excitation of acoustic fields for ultrasonic particle manipulation," *pubs.rsc.org*, Accessed: Oct. 30, 2022. [Online]. Available: https://pubs.rsc.org/en/content/articlehtml/2012/lc/c1lc20913b?casa_token=vLUcepWzAu

oAAAAA:bAzCPVQ_gunIpyfOrHMh6YDt005q56MKXyjt17QjzJULqJUc-LVFxFSZK_YhGL6C1ZjmurmQb1Wc

[67] D. Collins, A. Neild, Y. A.-L. on a Chip, and undefined 2016, "Highly focused high-frequency travelling surface acoustic waves (SAW) for rapid single-particle sorting," *pubs.rsc.org*, Accessed: Oct. 30, 2022. [Online]. Available: https://pubs.rsc.org/en/content/articlehtml/2016/lc/c5lc01335f?casa_token=cr4MERXakHMAAAAA:jXQBVVuA61Fm0IYwmEVeCqp9kx0XAEh5dN2DVSvp4Kju-CAzFkPfog20P3LVlgnhoa0Z8ajob_3r

[68] R. S. Weis and T. K. Gaylord, "Lithium niobate: Summary of physical properties and crystal structure," *Applied Physics A Solids and Surfaces*, vol. 37, no. 4, pp. 191–203, Aug. 1985, doi: 10.1007/BF00614817.

[69] A. A. Bent and N. W. Hagood, "Piezoelectric Fiber Composites with Interdigitated Electrodes," *http://dx.doi.org/10.1177/1045389X9700801101*, vol. 8, no. 11, pp. 903–919, Jul. 2016, doi: 10.1177/1045389X9700801101.

[70] R. Ehret, W. Baumann, M. Brischwein, A. Schwinde, K. Stegbauer, and B. Wolf, "Monitoring of cellular behaviour by impedance measurements on interdigitated electrode structures," *Biosens Bioelectron*, vol. 12, no. 1, pp. 29–41, Jan. 1997, doi: 10.1016/0956-5663(96)89087-7.

[71] D. Mandal, S. B.- Sensors, and undefined 2022, "Surface acoustic wave (SAW) sensors: Physics, materials, and applications," *mdpi.com*, vol. 22, p. 820, 2022, doi: 10.3390/s22030820.

[72] K. Länge, B. E. Rapp, and M. Rapp, “Surface acoustic wave biosensors: A review,” *Anal Bioanal Chem*, vol. 391, no. 5, pp. 1509–1519, Jul. 2008, doi: 10.1007/S00216-008-1911-5.

[73] K. Länge, B. E. Rapp, and M. Rapp, “Surface acoustic wave biosensors: A review,” *Anal Bioanal Chem*, vol. 391, no. 5, pp. 1509–1519, Jul. 2008, doi: 10.1007/S00216-008-1911-5.

[74] K. Yosioka, Y. K.-A. A. united with Acustica, and undefined 1955, “Acoustic radiation pressure on a compressible sphere,” *ingentaconnect.com*, Accessed: Oct. 30, 2022. [Online]. Available: https://www.ingentaconnect.com/content/dav/aaua/1955/00000005/00000003/art00004

[75] I. H. Karampelas and J. Gómez-Pastora, “Novel Approaches Concerning the Numerical Modeling of Particle and Cell Separation in Microchannels: A Review,” *Processes 2022, Vol. 10, Page 1226*, vol. 10, no. 6, p. 1226, Jun. 2022, doi: 10.3390/PR10061226.

[76] K. B.-J. of S. and vibration and undefined 1984, “Acoustic radiation pressure in the near field,” *Elsevier*, Accessed: Oct. 30, 2022. [Online]. Available: https://www.sciencedirect.com/science/article/pii/0022460X8490422X

[77] P. B. Muller and H. Bruus, “Theoretical study of time-dependent, ultrasound-induced acoustic streaming in microchannels,” *Phys Rev E Stat Nonlin Soft Matter Phys*, vol. 92, no. 6, Dec. 2015, doi: 10.1103/PHYSREVE.92.063018.

[78] N. Nama, R. Barnkob, Z. Mao, C. Kähler, F. C.-L. on a Chip, and undefined 2015, “Numerical study of acoustophoretic motion of particles in a PDMS microchannel driven by surface acoustic waves,” *pubs.rsc.org*, Accessed: Oct. 30, 2022. [Online]. Available: https://pubs.rsc.org/en/content/articlehtml/2015/lc/c5lc00231a?casa_token=oGGFgHhR_0

wAAAAA:1hLp5oxdkHNCynqv9MUK3sBm7evZjIKl3FdnFhnYUFe7zf44AvuxYgB8vp
HFALrcBSMYAA3P1xQd

[79] B. Talebjedi, M. Heydari, … E. T.-… in bioengineering and, and undefined 2022, "Neural Network-Based Optimization of an Acousto Microfluidic System for Submicron Bioparticle Separation," *ncbi.nlm.nih.gov*, Accessed: Oct. 30, 2022. [Online]. Available: https://www.ncbi.nlm.nih.gov/pmc/articles/PMC9061962/

[80] Z. Ma, A. J. T. Teo, S. H. Tan, Y. Ai, and N. T. Nguyen, "Self-Aligned Interdigitated Transducers for Acoustofluidics," *Micromachines 2016, Vol. 7, Page 216*, vol. 7, no. 12, p. 216, Nov. 2016, doi: 10.3390/MI7120216.

[81] D. Collins, R. O'Rorke, A. Neild, J. Han, Y. A.-S. Matter, and undefined 2019, "Acoustic fields and microfluidic patterning around embedded micro-structures subject to surface acoustic waves," *pubs.rsc.org*, Accessed: Oct. 29, 2022. [Online]. Available: https://pubs.rsc.org/en/content/articlehtml/2019/sm/c9sm00946a?casa_token=-wcr7Bs3f_sAAAAA:n_m0zH6-EV0cuPX2Z-EH8VqEMKjrLcDRUYDdyfD1Rzvo43ujpDIbpBLh1OY_lvketO3oBwAgB8ER